

<https://doi.org/10.1038/s41529-025-00652-0>

Evaluation of low-carbon cementitious composites in marine environment for coastal protection and artificial reef substrate



Adhora Tahsin¹, Ishrat Baki Borno¹, Nishad Ahmed¹, Nithya Nair¹, Warda Ashraf¹ ✉ & Christopher Hollenbeck²

This study investigates the long-term durability, microstructural evolution, and biological receptivity of three cementitious materials—Ordinary Portland Cement (OPC), Alkali-Activated Material (AAM), and Recreated Roman Cement (RRC)—under natural marine exposure for one year. A comprehensive bottom-up approach was employed, starting with microstructural characterization using XRD, MIP, microCT, TGA, SEM, and FTIR. These analyses were followed by evaluations of mechanical performance, carbon footprint, and biological growth potential. After one year, OPC paste samples exhibited ettringite, thaumasite, and gypsum formation, causing full-depth cracks. Despite this, OPC mortar maintained the highest compressive strength (70 MPa) among all binders. In contrast, RRC showed no ettringite or thaumasite formation; only increased hydrotalcite formation at its edges was observed. Nevertheless, RRC achieved a strength level comparable to OPC (55 MPa). Sodium hydroxide-activated blast furnace slag was used as the AAM composite for this study. The tested AAM formulation imparted the lowest compressive strength (35 MPa), attributed to the drying shrinkage crack formation during the initial sealed curing, which exacerbated upon seawater exposure. Notably, AAM showed increased calcium silicate hydrate (C-S-H) formation with time. Both RRC and AAM mortars exhibited lower environmental footprints, achieving reductions in global warming potential (GWP) of 50% and 52%, respectively, compared to OPC.

Global freshwater scarcity is raising concerns about the availability of potable water for mixing and curing concrete^{1,2}, making it necessary to rely on seawater, which constitutes 97% of the total water on Earth³. As the leading concrete producer, China intensifies this issue by requiring 27.53 billion tons of freshwater annually to support its booming construction industry and coastal construction projects^{4,5}. Meanwhile, directly using seawater in concrete is not viable due to its detrimental effects on conventional material durability. Ordinary Portland Cement (OPC), the most widely used binder, is vulnerable to seawater-induced degradation⁶, and is responsible for about 8% of global anthropogenic CO₂ emissions^{7,8}. Therefore, it is urgent to develop a cementitious material that is both durable in seawater and has a low carbon footprint to enhance the longevity of maritime structures, such as artificial islands, land reclamation projects, large floating platforms, and artificial reefs⁹.

Cement-based materials like OPC, pozzolanic blended cement (PBC), and alkali-activated material (AAM) undergo chemical reactions with aggressive ions present in seawater, causing both chemical and physical damage to marine concrete structures¹⁰. Common deterioration processes include salt crystallization, expansive phase formations, cement hydrate decomposition, and surface abrasion¹¹. Sulfate (SO₄²⁻) ions in seawater initiate a severe chemical reaction in hardened concrete, forming ‘delayed ettringite’ and gypsum, ultimately causing crack formation by volume expansion^{12,13}. Notably, SO₄²⁻, magnesium (Mg²⁺), and chloride (Cl⁻) ions increase Ca(OH)₂ consumption in the OPC system and contribute to the degradation of C-S-H, which is the primary binding phase of the OPC matrix¹⁴. Sodium (Na⁺) and potassium (K⁺) ions in seawater can also react with active silica (Si) in aggregate to form alkali-silica reaction (ASR) products, affecting durability¹⁵. The reaction mechanism of AAM differs from

¹Department of Civil Engineering, The University of Texas at Arlington, Nedderman Hall, Arlington, TX, USA. ²Department of Life Sciences, Texas A&M AgriLife Research and Texas A&M University—Corpus Christi, Corpus Christi, TX, USA. ✉e-mail: warda.ashraf@uta.edu

OPC as they lack portlandite and have scarce gypsum and ettringite formation when exposed to seawater¹⁶. The AAM system prepared with the alkali-activation of blast furnace slag or fly ash is suitable for marine environments due to its ability to bind Cl^- , increasing pore refinement and enhanced chemical stability of C-(N)-A-S-H and C-S-H with low Ca/Si^{16,17}. However, the long-term strength loss in AAM systems, caused by the degradation of C-S-H through carbonation, remains a significant concern¹⁸. To create a binder suitable for marine applications with a low carbon footprint, a novel binder was developed combining calcined clay, lime, and seawater inspired by the Roman cement system, named 'Recreated Roman Cement (RRC)'^{19,20}. Ancient Roman marine structures (e.g., seawalls and harbor piers) were highly durable and withstood the harsh marine environment for 2000 years^{11,21}. The RRC binder showed its ability to efficiently bind Cl^- and SO_4^{2-} from seawater²⁰ and can significantly lower the carbon footprint of OPC production^{22,23}.

Critical attention to cementitious material selection is also necessary when concrete is used as the substrate for artificial reef production. Low-alkaline concrete enables rapid oyster colonization and supports healthy populations of oyster spat and juveniles, promoting a vibrant marine ecosystem^{24,25}. However, OPC has high alkalinity, with a pH of around 13 compared to seawater's pH of approximately 8, creating a poor substrate for biological recruitment and introducing toxic compounds that can be harmful to marine life²⁵. Microalgae readily adhere to pH-neutral materials, like silica-enriched (pozzolanic) cement, blast-furnace slag, and fly ash, along with mixtures of these with OPC; additionally, carbonated cement typically exhibits superior algae attachment rates compared to conventional materials^{25,26}. Marine organisms interact with concrete in two ways: bio-fouling and bio-protection. Algal filaments can damage the concrete surface, while barnacles and oyster crusts offer protection by sealing microcracks, particularly against Cl^- attacks^{27–29}. Biofilm coating by these organisms reduces the Cl^- ion permeability and mortar carbonation, thereby enhancing the reinforced concrete (RC) structure durability in tidal zones^{30,31}.

This study aims to characterize various cementitious materials to evaluate their performance in marine environments. This evaluation focuses on three key aspects: (i) durability against seawater ions, (ii) reduction of the carbon footprint, and (iii) potential for creating substrates suitable for artificial reef systems. As the conventional binder, the microstructural changes in OPC systems and their impact on mechanical properties under long-term seawater exposure have been extensively investigated in previous literature^{32,33}. Conversely, while some studies have examined the use of seawater in mixing and curing AAM mixes^{18,34,35}, showing improved compressive strength and enhanced resistance to sulfate attack, the effects of long-term exposure to natural marine environments remain largely unexplored. Lastly, RRC is a novel cementitious system, relying on seawater activation and the pozzolanic reaction between calcined clay and lime. Preliminary investigations into its microstructure suggest strong potential for durable marine concrete^{19,20,36}. Consequently, assessing the long-term durability of RRC under natural seawater exposure is crucial. A bottom-up approach was employed, starting with an analysis of the microstructural evolution of these different cementitious systems under natural marine conditions. Techniques such as X-ray diffraction analysis (XRD), mercury intrusion porosimetry (MIP), X-ray micro-computed tomography (microCT), thermogravimetric (TGA) analysis, scanning electron microscopy (SEM), and Fourier transform infrared (FTIR) spectroscopy were utilized. These microstructural assessments were then followed by evaluations of mechanical performance, carbon footprint, and bio-receptivity.

Results

Mineralogy of different binder systems under seawater exposure

Figure 1 shows the mineral formation in different paste samples before exposure and after 1 month, 5 months, and 1 year of natural seawater exposure. Portlandite added as a raw material in the RRC mix reacted with Al and Si from calcined clay and was completely consumed, with no traces remaining even after 28 days of laboratory curing (Fig. 1a). As per the previous study, pozzolanic reactivity between calcined clay and lime should

form C-S-H, C_2ASH_8 (stratlingite), and tetracalcium aluminate hydrates (C_4AH_{13})³⁷. Due to the incorporation of seawater, hydrocalumite formation was observed at 11.4° (2 theta), resulting from the binding of Cl^- by C_4AH_{13} (Fig. 1a)^{38,39}. The peak at 29° (2theta) can be because of several phases, including C-S-H^{40,41}, calcite, gypsum, and katoite. Among the other crystalline formations, quartz was evident in RRC mixes due to using medium-grade kaolin clay^{22,42}. $\text{Mg}(\text{OH})_2$ was present in hydrated lime used to produce RRC (Table 1). Consequently, brucite ($\text{Mg}(\text{OH})_2$) was observed in these clay mixes from the early hydration period (Fig. 1). Throughout the exposure period, the XRD analysis revealed no significant changes in the RRC sample.

In OPC paste (Fig. 1b), calcium aluminate monosulfate formation was observed before exposure to natural seawater. The hydration of C_3A in the presence of gypsum ($\text{CaSO}_4 \cdot 2\text{H}_2\text{O}$) leads to the formation of ettringite ($\text{Ca}_6\text{Al}_2(\text{SO}_4)_3(\text{OH})_{12} \cdot 26\text{H}_2\text{O}$)⁴³. Over time, as the gypsum is consumed, the ettringite gradually transforms into monosulfate ($\text{Ca}_4\text{Al}_2\text{O}_6(\text{SO}_4) \cdot 12\text{H}_2\text{O}$)⁴³. Due to the SO_4^{2-} ion abundance in natural seawater, this mineral eventually transformed into ettringite at later stages⁴⁴. OPC hydration continuously produced portlandite⁴⁴. The SO_4^{2-} ions from seawater also reacted with Ca^{2+} ions released from this portlandite and produced gypsum. Moreover, soluble carbonates in seawater gave rise to calcite and thaumasite in the OPC sample after 5 months and 1 year of exposure. Thaumasite is known to form at low temperatures^{32,45}, and is a non-cementitious product resulting from the reaction between CaCO_3 , gypsum, and C-S-H³². So, while enduring a winter season during the exposure period, thaumasite was produced in the OPC sample (23.39° two-theta).

In alkali-activated materials (AAM), a sufficiently high concentration of hydroxide ions is necessary to dissolve adequate amounts of Ca, Al, and Si from slag, while metal cations are essential for charge balancing within the product phase⁴⁶. The primary reaction products have been identified as C-S-H/C-A-S-H phases, calcite, and tetracalcium aluminate hydrate (C_4AH_{13}) (Fig. 1c)^{18,41}. The peak at 29.6° for this sample was sharp before exposure, but broadened as the natural seawater exposure duration increased. The increase in amorphous C-S-H content likely contributed to the broadening of this peak. Before exposure to natural seawater, prominent peaks corresponding to C_4AH_{13} were observed at 27.1° , 32.85° , 36° , 47.6° , 48.6° , 49.9° . However, after one year, these peaks disappeared, with only peaks at 11.6° and 23.2° remaining, suggesting the possible presence of both C_4AH_{13} and hydrocalumite. This indicates that the abundance of chloride ions in seawater facilitated the transformation of C_4AH_{13} into hydrocalumite¹⁸.

Pore structure of different binder systems under seawater

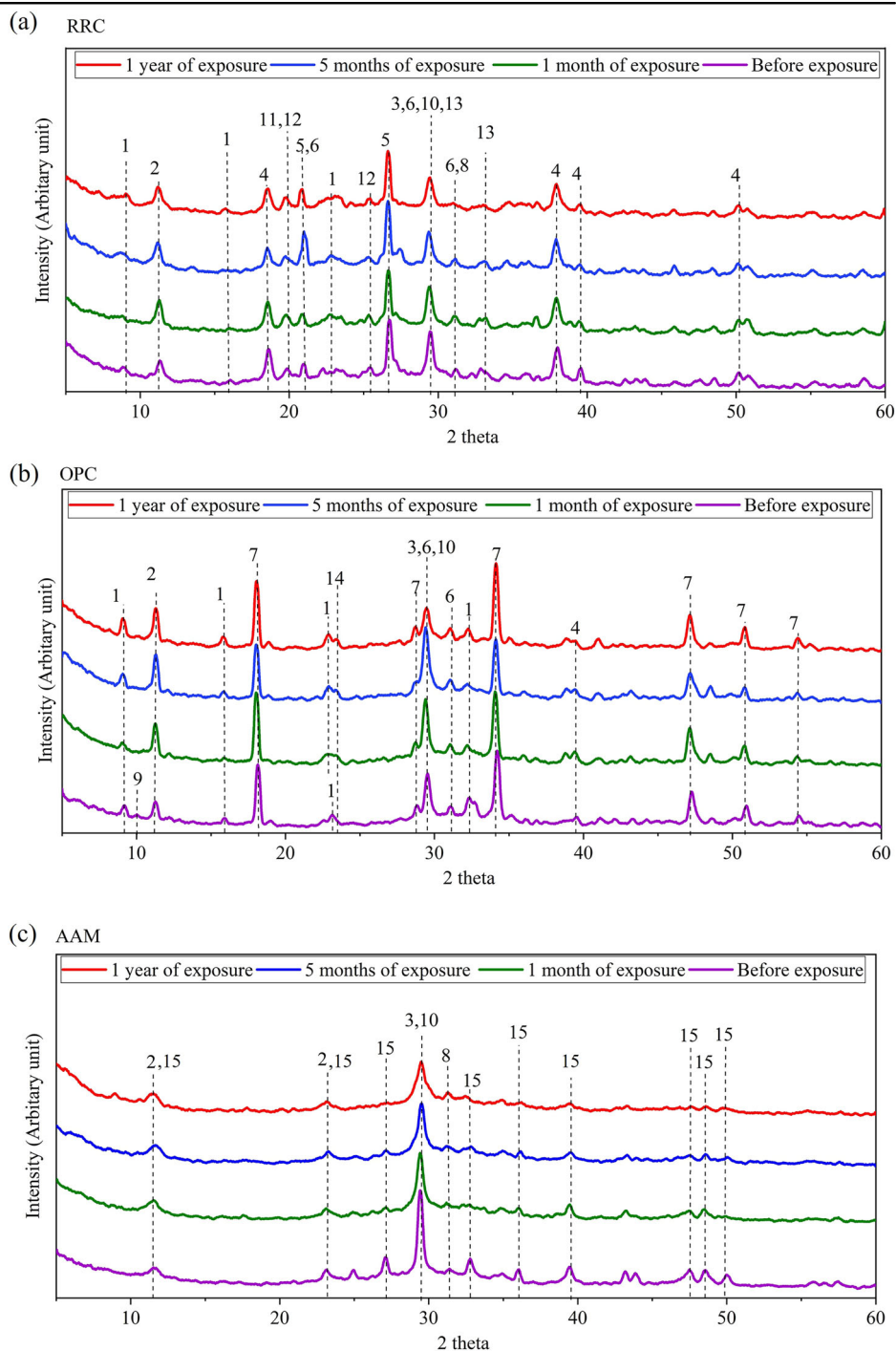
Figure 2a–c depicts the quantification of the cumulative porosity combining mesopores (radius 2–50 nm) and macropores (>50 nm)⁴⁷ across different samples before exposure, and after 1 month and 1 year of natural seawater exposure. Overall, the cumulative pore volume of the RRC sample remained constant over the exposure duration, around 0.18–0.2 ml/g, with a slight reduction after one year (Fig. 2a). The OPC sample initially exhibited a higher cumulative pore volume than RRC, totaling approximately 0.27 ml/g after 1 month of exposure (Fig. 2b), attributed to its higher water/cement ratio (Table 2). However, after 1 year, the total pore volume of OPC reduced to 0.18 ml/g, possibly due to the continuous cement hydration and ettringite formation filling out the pores. The cumulative pore volume of AAM ranged from 0.07–0.1 ml/g, which was the lowest among all the different binder systems (Fig. 2c), indicating a dense microstructure.

Figure 2d–f show the changes in the pore size distribution of the samples before exposure, after 1 month, and after 1 year of natural seawater exposure. Since the minimum detectable pore diameter of the MIP instrument used in this study was 5 nm, the measured pore sizes for all three cementitious systems ranged from 5 to 110 nm. As per previous literature, pore diameters ranging from 3.75–5 nm correspond to pores in compact C-S-H, 5–40 nm refer to less compact C-S-H connected to larger capillary pores, 40–100 nm include capillary pores and microcracks, and above 100 nm indicate large capillary pores and defects⁴⁸. RRC depicted only one critical pore diameter, ranging from 5–40 nm⁴⁹ (Fig. 2d),

Table 1 | Oxide contents (mass %) of the raw materials

| Raw material | Mass fraction w/% | | | | | | | |
|---------------------|--------------------------------|------------------|------|--------------------------------|-------------------|-------|-----------------|------------------|
| | Al ₂ O ₃ | SiO ₂ | CaO | Fe ₂ O ₃ | Na ₂ O | MgO | SO ₃ | K ₂ O |
| Medium-grade kaolin | 32.9 | 55.7 | 2.17 | 4.18 | 0.479 | 0.743 | 0.686 | 1.34 |
| Slag | 15.6 | 29.6 | 36.4 | 0.372 | 0.762 | 9.69 | 5.19 | 0.305 |
| Hydrated lime | 0.204 | 0.331 | 73.7 | 0.302 | - | 25.3 | 0.069 | - |
| OPC | 3.87 | 21.2 | 65.3 | 3.10 | - | 0.816 | 4.28 | 0.679 |

Fig. 1 | Mineralogical details in the different binder systems. Mineralogical details in (a) RRC, (b) OPC and (c) AAM binder systems before exposure and after 1 month, 5 months, and 1 year of natural seawater exposure. Here, 1: Ettringite-PDF-96-901-7147; 2: Hydrocalumite-PDF-96-900-9354; 3: Calcium silicate hydrate^{40,41}; 4: Brucite-PDF-96-101-0485; 5: Quartz-PDF-96-900-5020; 6: Gypsum-PDF-96-901-3167; 7: Portlandite-PDF-96-100-1769; 8: Akermanite-PDF-96-900-6451; 9: Monosulfate⁴⁰; 10: Calcite-PDF-96-210-0993; 11: Montmorillonite-PDF-96-901-0958; 12: Grossite-PDF-96-350-0015; 13: Katoite-PDF-96-900-2710; 14: Thaumasite-PDF-96-901-0880; 15: Tetra-calcium aluminate hydrate (C₄AH₁₃)⁴¹.



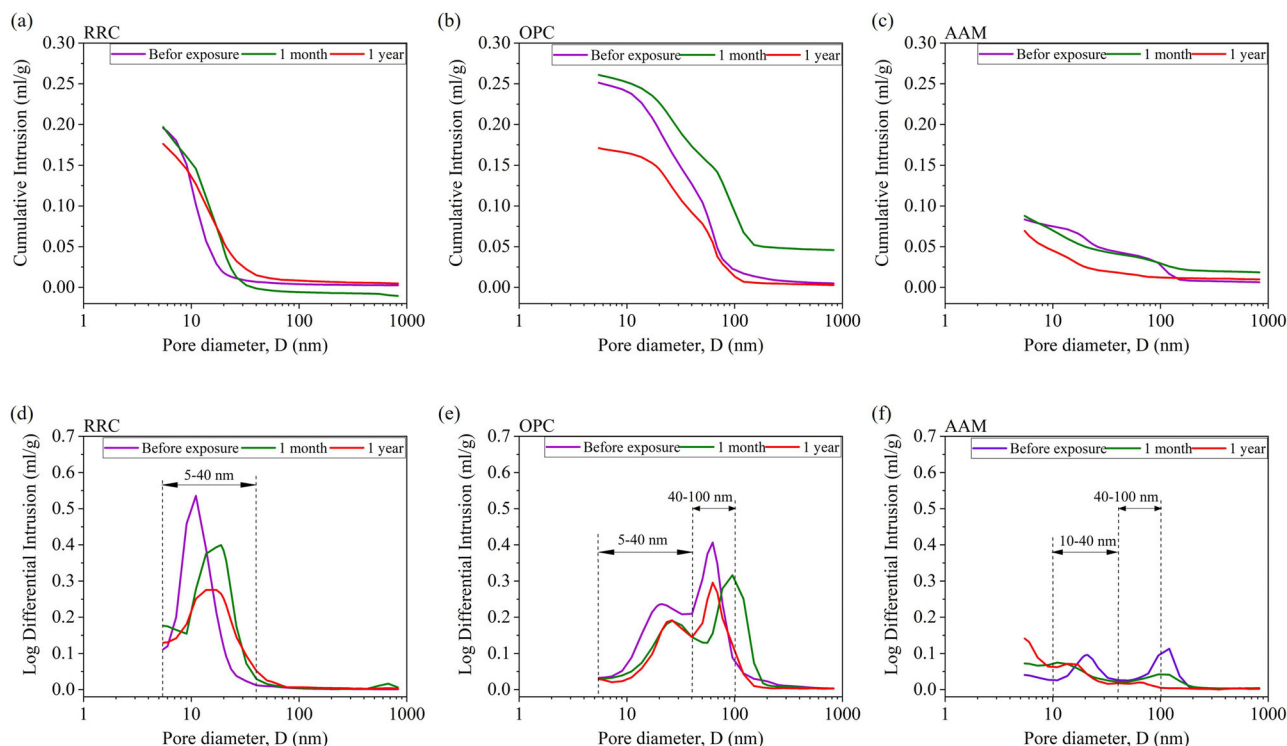


Fig. 2 | Cumulative intrusion and differential intrusion distribution of different binder systems. Changes in the pore distribution at different exposure durations to natural seawater. Cumulative intrusion of (a) RRC, b OPC, and (c) AAM sample, and differential intrusion distribution of (d) RRC, e OPC, and (f) AAM sample.

Table 2 | Mix design per 100 g of binder

| Mixes | Calcined Medium-grade clay (g) | Lime (g) | OPC (g) | Slag (g) | sand/binder | water/binder | Superplasticizer dosage |
|-------|--------------------------------|----------|---------|----------|-------------|--------------|-------------------------|
| RRC | 60 | 25 | 0 | 15 | 0.88 | 0.36 | 2% |
| AAM | 0 | 0 | 0 | 100 | 3 | 0.5 | 0 |
| OPC | 0 | 0 | 100 | 0 | 2.75 | 0.66 | 0 |

indicating minimal capillary pores due to the tight packing of gel and crystalline phases. Over time, the critical pore diameter increased, likely due to the crystallized phase growth from prolonged seawater exposure and leaching of ions. For OPC and AAM, two critical pore diameters were observed: one at around 5–40 nm and another at 40–100 nm (Fig. 2e, f). The medium capillary pore induced in the OPC matrix before exposure to natural seawater can be due to its higher water/binder ratio. Upon seawater exposure, the ion influx led to mineral formation in OPC (Fig. 1b, XRD analysis). This initially increased the critical diameter of the capillary pores after one month, but after 1 year, this diameter reduced (Fig. 2e). As shown in the TGA plot (Fig. S1b, Supplementary section), the hydration product formation in the OPC matrix continued to increase over time, reaching a maximum at one year. These hydration products precipitated within the capillary voids, progressively filling them and thereby reducing the critical pore diameter⁵⁰. Capillary voids were also observed in AAM prior to natural seawater exposure (Fig. 2f); however, the volume of the pores in this region is much lower than that observed in the OPC system. After 1 year of exposure, the peaks in the pore size range of 10–100 nm decreased; instead, a new critical pore diameter of 5 nm emerged, indicating gel pore formation. Fig. S1c (Supplementary section) also confirms that C-S-H/C-A-S-H precipitation in the AAM system significantly increased after one year of exposure to seawater. This suggests that the initially slow hydration of AAM led to the presence of larger pores, which were progressively filled over time with gel phases such as C-S-H/C-A-S-H, thereby refining the pore structure and enhancing the microstructural integrity¹⁸.

Evolution of microstructure observed from cross-sectional analysis

MicroCT image analysis was performed to investigate microstructural changes and the distribution of large pores or air voids with diameters exceeding 60 μm in various binder systems after 1 month and 1 year of natural seawater exposure (Fig. 3). Both the grayscale and color images in Fig. 3 depict the pixel intensity variation along the cross-section (XZ plane), with the color gradient displayed at the top. The darker blue shade represents the pixels with lower light intensity, while the brighter colors on the right indicate pixels with higher light intensity (Fig. 3).

The RRC paste samples did not show any major crack up to 1-year exposure duration (Fig. 3a), attributed to the lack of portlandite content, and the mineral formations sequestering SO_4^{2-} and Cl^- during the initial hydration stage (Fig. 1a). Moreover, the color image of the RRC cross-section (Fig. 3a-iii) showed a bluish outer rim formation at the initial stage of seawater exposure (1 month). After 1 year, this blue rim expanded, and an additional greenish rim developed outside of it (Fig. 3a-iii). To investigate the reason for the bluish-colored zone, a small sample measuring around 4–5 μm on each side was taken from the peripheral region of the 25 \times 25 \times 25 mm^3 paste sample; the microCT analysis of this sample yielded images with 9 μm resolution (Supplementary section, Fig. S2). Segmenting two cylindrical volumes (22.5 mm^3) from this high-resolution 3D image revealed that the bluish area has a porous matrix with a pore volume of 0.27 mm^3 , while the greenish area is denser with a pore volume of 0.11 mm^3 (Supplementary section, Fig. S3). Therefore, even though RRC samples did not crack after 1 year of exposure, the outer layer of these composites became

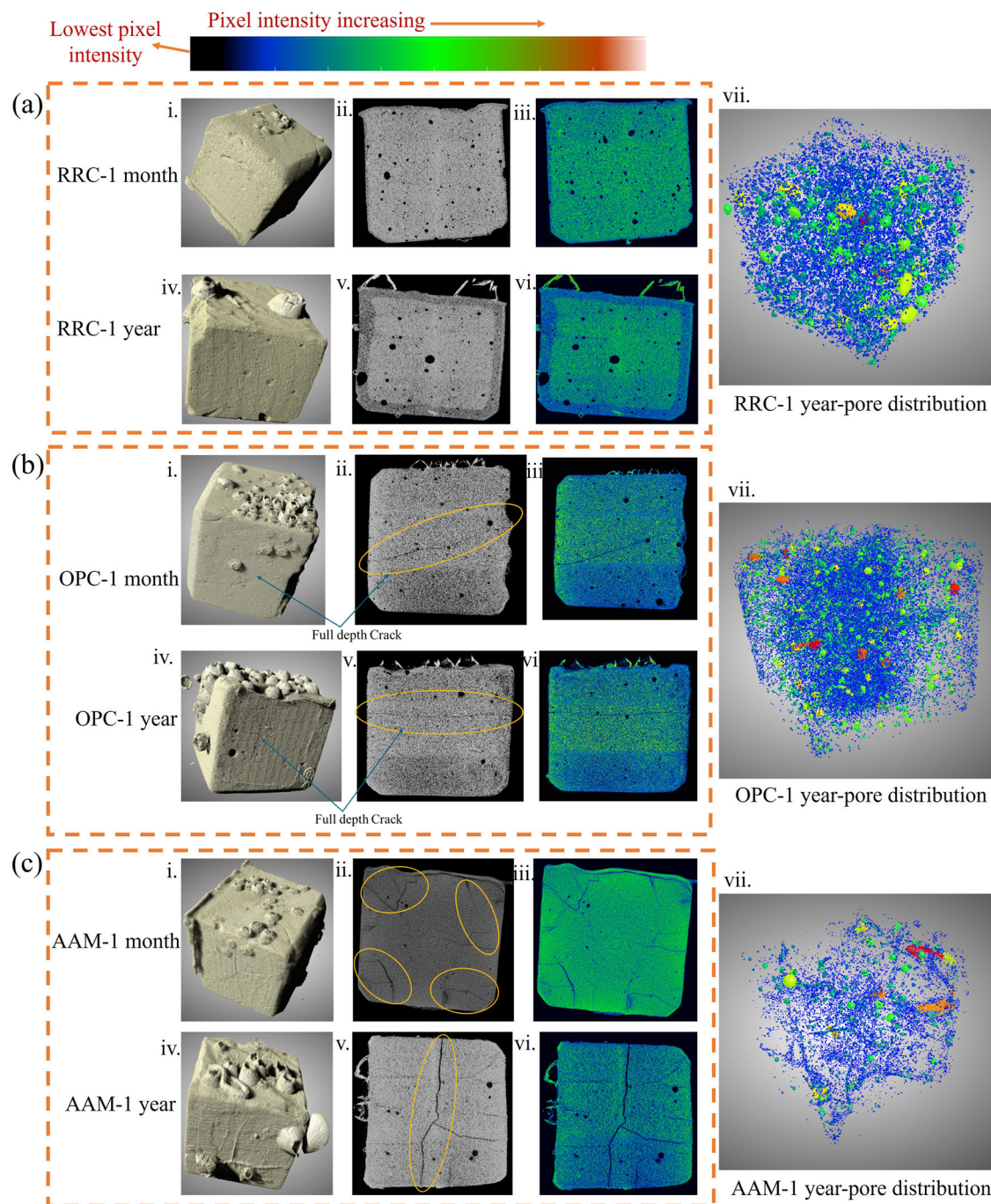


Fig. 3 | Visualization of the 1-month and 1-year seawater exposed paste sample microstructure and the air void (diameter > 60 μm) distribution in the 1-year sample. Microstructural changes visualized in (a) RRC, (b) OPC, and (c) AAM

sample from the pixel intensity variation in the greyscale and color cross-sectional images. Air void distribution in (a-vii) RRC, (b-vii) OPC, (c-vii) AAM.

Table 3 | Global warming potential of different materials

| Raw materials | Global warming potential (kg CO ₂ eq/kg) |
|-------------------|---|
| Medium grade clay | 0.032 |
| Hydraulic lime | 0.540 |
| OPC | 0.915 |
| Slag | 0.091 |
| Superplasticizer | 1.530 |
| Sand | 0.012 |
| Water | 0.002 |

more porous with time. Such an increase in porosity could be due to two mechanisms: (i) element leaching from the matrix to seawater and (ii) gel phase conversion to crystalline products, reducing molecular volume. Further microstructural analysis is necessary to confirm the variations in product formation within these rims. Additionally, microCT pore distribution analysis of the RRC sample quantified the total air void volume to be 33 mm³, which constitutes 0.55% of the total sample volume (pore diameter: 0.06–1.86 mm) (Fig. 3a-vii).

As shown in Fig. 3b, OPC paste samples showed full-depth crack formation at both exposure durations (1 month and 1 year). This cracking can be attributed to the continuous ettringite and gypsum formation over time (Fig. 1b), as ettringite can expand by absorbing

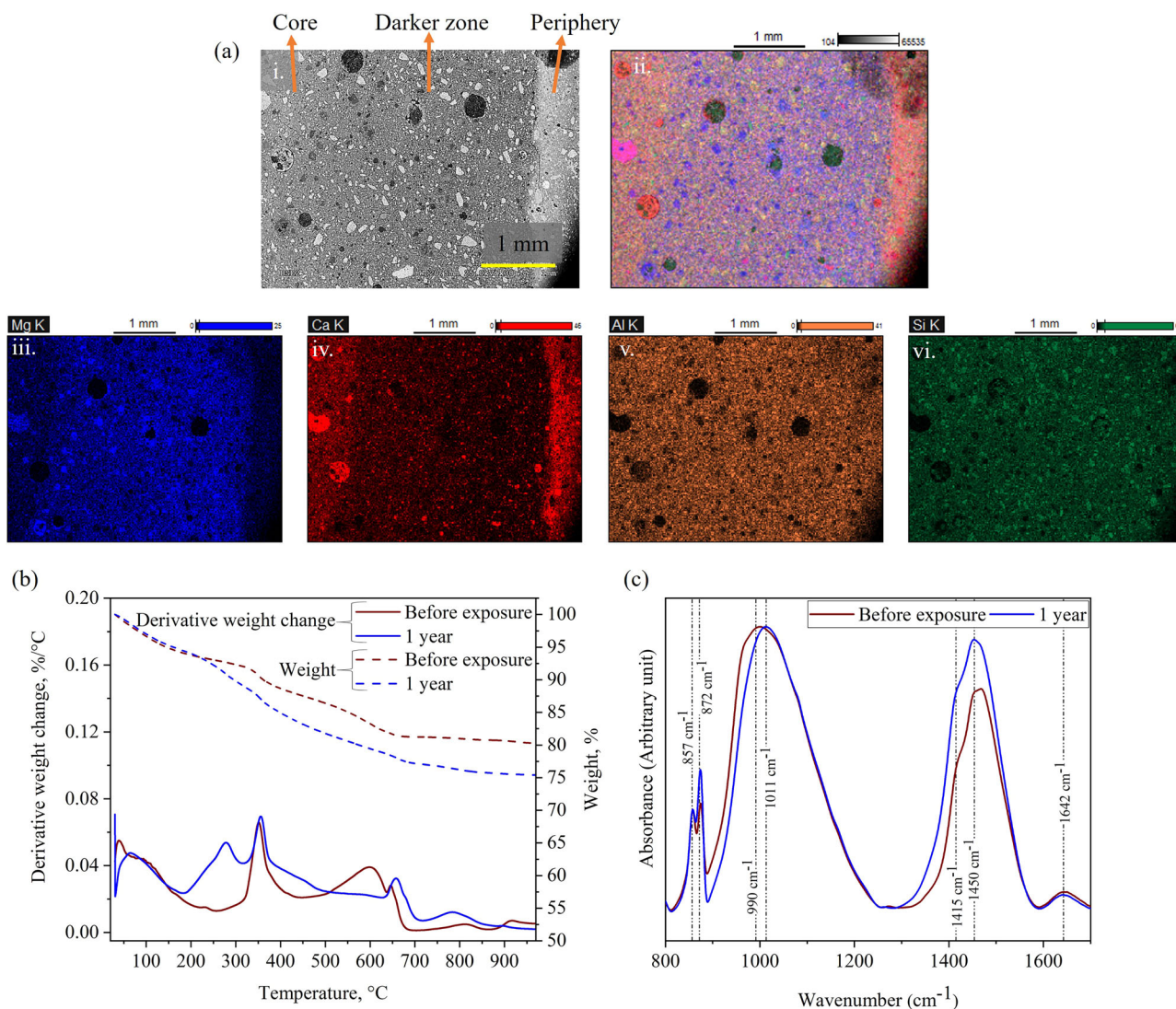


Fig. 4 | Compositional evolution in the RRC peripheral region under 1-year seawater exposure. **a** Elemental variation (1-year exposure), **b** TG-DTG curve (before exposure and 1-year exposure), and **c** FTIR spectra (before exposure and 1-year exposure) of the RRC peripheral region.

water and damage the concrete microstructure⁶. The total air void volume of the OPC sample was lower than that of the RRC sample, measuring 15.22 mm³, which constitutes 0.24% of the total sample volume (pore diameter range: 0.06–0.82 mm) (Fig. 3b-vii). Also, as per the pore distribution analysis, the peripheral region had fewer small-diameter pores (denser blue dots at the core than the periphery).

After 1 month of exposure, the AAM paste samples exhibited extensive cracking originating from the surface (Fig. 3c-i, ii, iii), indicating them to be shrinkage cracks. Such shrinkage cracks may have formed at the early-age during sealed curing and before SW exposure. Following 1 year of exposure, the shrinkage cracks expanded and merged, completely fracturing the sample (Fig. 3c-iv, v, vi). At this point, the AAM paste sample was extremely weak and crumbled with minimal tapping. This weakness can be attributed to drying shrinkage during the initial sealed curing period (before exposure), leading to crack formation, which propagated over time⁵¹. AAM is susceptible to drying shrinkage primarily due to the lack of crystal phases like portlandite and the C-A-S-H characteristics⁵². The high alkali dosage (5% Na₂O) likely increased slag dissolution¹⁷, resulting in dense gel precipitation with a fine pore structure, as indicated by MIP analysis (Fig. 2c). This led to high capillary pressures during drying, significantly enhancing shrinkage in this sample⁵². The total air void volume in AAM was the lowest among all cementitious systems, measuring 5.16 mm³,

constituting 0.07% of the total sample volume (pore diameter: 0.06 ~ 1.58 mm) (Fig. 2c-vii).

Compositional variation in the peripheral region

When cementitious composites are submerged in seawater, ions begin to permeate from the outer regions. Consequently, the most significant changes occur in this area, and identifying microstructural evolution can be achieved by observing the changes in mineral composition there. To investigate this, BSE-EDS with areal mapping was initially used to analyze the elemental variations in the outer regions of different binder systems. Following this, TGA and FTIR were employed to confirm the changes in the gel and mineral phases.

As observed from the BSE image in Fig. 4a-i, the outermost region of the 1-year seawater-exposed RRC sample appeared bright. A darker layer existed on the left of this zone; it became greyish further to the left towards the core. The atomic area mapping in Fig. 4a-ii shows that the peripheral region (on the right) was rich in calcium (Ca) with no magnesium (Mg) presence (Fig. 4a-iii, iv). In contrast, the darker zone was rich in Mg and lacked Ca (Fig. 4a-iii, iv). Towards the core of the sample, the Ca levels increased again while Mg levels decreased (Fig. 4a-iii, iv). The aluminum (Al) and silicon (Si) content remained consistent across all three zones (Fig. 4a-v, vi). This phenomenon can be linked to findings from the micro-CT analysis (Supplementary section, Fig. S4a, b). The dark area in the BSE

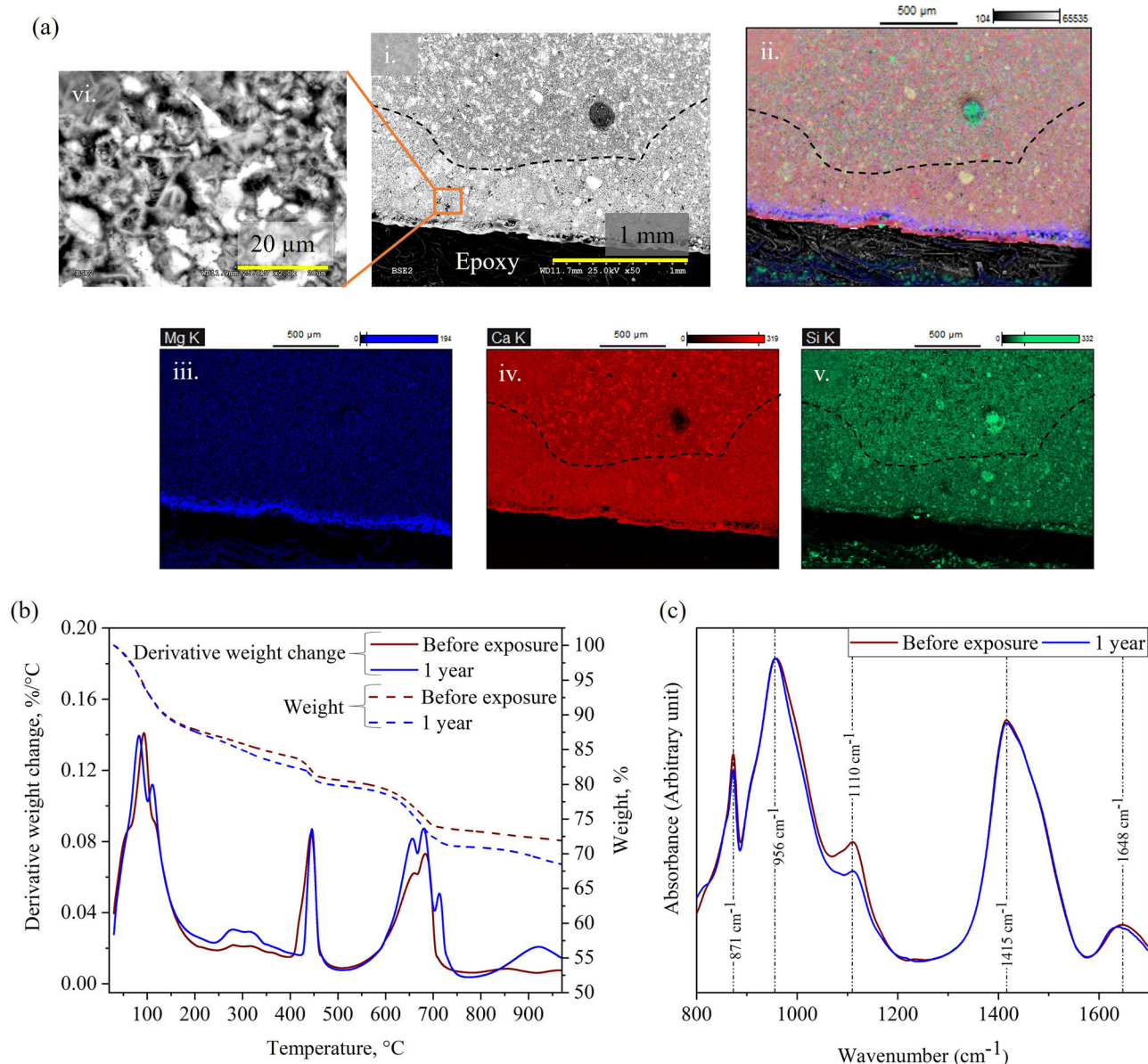


Fig. 5 | Compositional evolution in the OPC peripheral region under 1-year seawater exposure. **a** Elemental variation (1-year exposure), **b** TG-DTG curve (before exposure and 1-year exposure), and **c** FTIR spectra (before exposure and 1-year exposure) of the OPC peripheral region.

image corresponds to the porous blue zone in the microCT image, while the lighter peripheral area matches the thin green layer at the microCT sample boundary. The elemental mapping (Supplementary section, Fig. S4c) revealed that in the darker zone, the Mg/(Al+Si) ratio ranged from 0 to 2; in contrast, in the peripheral region and at the core of the sample, this ratio varied from 0 to 0.5. Conversely, the Ca/(Al+Si) ratio in the darker zone was low, ranging from 0 to 0.2, while the ratio in the other two zones ranged from 0.1 to 1.1.

The TGA analysis of the RRC peripheral region in Fig. 4b indicates that before exposure to natural seawater, there was significant weight loss between 500–680 °C, along with a minor hump at 800 °C. According to the literature, calcite, the most thermodynamically stable calcium carbonate (CaCO₃) polymorph, decomposes at 720–875 °C; in contrast, the less stable polymorphs, vaterite and aragonite, decompose at 550–675 °C and 675–720 °C, respectively⁵³. Therefore, the weight loss in the before exposure sample between 500–680 °C was attributed to the less stable CaCO₃ polymorph decomposition, with some stable calcite decomposition at 800 °C (Fig. 4b). After 1 year of exposure, only the weight loss between 650–700 °C and around 800 °C was observed,

indicating the conversion of less stable CaCO₃ into the more stable form. Moreover, the 1-year sample displayed significant weight loss between 200–300 °C and 350–450 °C, likely due to hydrotalcite dehydroxylation⁵⁴, which was not identified in the before-exposure sample. However, brucite decomposition was observed in the before-exposure sample between 340–400 °C⁵⁵ reduced after 1 year of exposure, suggesting its conversion to hydrotalcite.

Confirming the TGA results, less stable aragonite presence in the before-exposure sample was verified in the FTIR analysis through the asymmetric stretching vibration (ν_3) and in-plane bending vibration (ν_2) of CO₃²⁻ at ~1450 cm⁻¹ and 857 cm⁻¹. Moreover, the calcite peak observed from the asymmetric stretching vibration (ν_3) and in-plane bending vibration (ν_2) of CO₃²⁻ at 1415 cm⁻¹ and 872 cm⁻¹ became sharper with the exposure duration^{47,56}. The FTIR spectra also exhibited a broad absorption between 800 cm⁻¹ and 1200 cm⁻¹, corresponding to the asymmetrical stretching vibration (ν_3) of the Si-O bond⁵⁷. The before-exposure spectra show a broader peak for Q₃ polymerization of silicates at around 990 cm⁻¹, which shifted to 1011 cm⁻¹ and became sharper after 1 year, indicating increased silica polymerization.

The BSE image showing the area mapping of the peripheral region of the OPC sample, exposed to seawater for 1 year, is presented in Fig. 5a. The outermost zone (beside epoxy) of the sample was Ca-rich (red layer, Fig. 5a-ii, iv); the EDS spectra confirm this zone to be a CaCO_3 layer (Supplementary section, Fig. S5a-ii). A Mg-rich layer, identified as a MgCO_3 layer by EDS (Supplementary section, Fig. S5a-i), was observed adjacent to this zone (blue layer, Fig. 5a-ii, iii). The zone near this MgCO_3 layer was observed to be somewhat porous; a magnified image of a small area from this zone is illustrated in Fig. 5a-vi. This zone is notably rich in Ca and low in Si; for clarity, this area has been marked with dotted lines (Fig. 5a-i, ii, iv, v). The BSE-EDS analysis identified this porous area as consisting of crystalline phases (Supplementary section, Fig. S5b). The needlelike phase had a similar composition as the thaumasite-ettringite solid solution⁵⁸, containing Ca, Si, Al, Cl, and sulfur (S) with high Ca/Si (Ca/Si ~ 4) (Supplementary section, Fig. S5b-i). The whitish products contained Ca, Al, and Cl, like the composition of hydrocalumite (Supplementary section, Fig. S5b-ii).

Thaumasite generally undergoes a four-step weight loss, with the initial loss at 133 °C attributed to loosely bound water, followed by OH^- group decomposition at about 450 °C, CO_2 loss at 720 °C, and SO_4^{2-} decomposition to $\text{SO}_2(\text{g})$ around 900 °C⁵⁹. The TGA analysis of the OPC peripheral region after 1-year exposure indicates a weight loss between 850–980 °C, along with distinctive weight loss at around 130 °C and 720 °C (Fig. 5b) indicating thaumasite decomposition. However, thaumasite decomposition was not observed in the before-exposure OPC sample. Ettringite decomposition at 100 °C and hydrocalumite decomposition between 250–350 °C⁵⁴ were noted in the OPC matrix both before exposure and after 1 year. Ettringite decomposition was significantly higher than hydrocalumite, indicating that the Cl^- bound in AFm was insufficient to reduce ettringite formation, eventually leading to thaumasite formation. Weight loss between 600–700 °C from CaCO_3 decomposition indicated an increase in CaCO_3 in the OPC binder system after 1 year of exposure (Fig. 5b). Apart from the TGA analysis, a characteristic SO_4^{2-} vibration at 1100 cm^{-1} indicated the presence of thaumasite and ettringite in this system (Fig. 5c). The CO_3^{2-} vibration at 1415 cm^{-1} is due to the presence of CaCO_3 and thaumasite in the matrix (Fig. 5c).

In the BSE images of the outer layer of the AAM, a whitish layer is visible next to a darker peripheral region (Fig. 6a-i). Area mapping reveals this whitish region to have a high Ca-concentration, represented as a dark red layer (Fig. 6a-ii, iv). Adjacent to this Ca-rich layer is another layer with higher Mg content, depicted as a dark blue layer (Fig. 6a-ii, iii). The intensity of Si and Al remained relatively uniform. TGA analysis showed CaCO_3 decomposition in the AAM sample after 1 year of seawater exposure, observed from the weight loss between 650–700 °C and 700–900 °C (Fig. 6b). Therefore, C-S-H carbonation may have allowed Mg to enter the gel phase, increasing M-S-H in the adjacent layer and creating a Mg-rich area (blue layer, Fig. 6a-ii, iii). A significant weight loss between 30–200 °C due to the C-S-H and C_4AH_{13} decomposition¹⁸ was noted in the sample before exposure (Fig. 6b). However, after 1 year, this weight loss peak became broader, while the weight loss increased between 250–450 °C because of hydrocalumite decomposition. This broadening of the 30–200 °C peak may have resulted from the conversion of C_4AH_{13} into hydrocalumite. Agreeing with the TGA results, the FTIR spectra in Fig. 6c also showed a Q_2 silica polymerization peak at 953 cm^{-1} , which was sharper in the pre-exposure spectra and became broader after one year. Furthermore, the calcite peak was confirmed in both pre-exposure and post-exposure FTIR spectra by observing the asymmetric stretching vibration (ν_3) and in-plane bending vibration (ν_2) of CO_3^{2-} at 1412 cm^{-1} and 871 cm^{-1} (Fig. 6c).

Mechanical performance

Figure 7a illustrates the seawater-exposed mortar compressive strength for up to 1 year. After 28 days of laboratory curing, the initial compressive strength for RRC, OPC, and AAM was observed to be 40, 45, and 34 MPa, respectively. Over time, both OPC and RRC samples showed a gradual increase in strength. Notably, during the one-year seawater exposure, the samples experienced a cold cycle, with surface water temperatures dropping

from 28–30 °C to around 16 °C during winter⁶⁰. However, neither sample exhibited any significant reduction in strength at the 1-year mark compared to the 5-month mark, indicating no adverse effect from the temperature drop. OPC samples demonstrated the highest strength, reaching 68 MPa after 1 year. Meanwhile, RRC samples also performed well, achieving a 55 MPa compressive strength after 1 year, 19% lower than the OPC mortar. The AAM mortar's compressive strength increased slightly after 5 months to 39 MPa, but decreased to 35 MPa after 1 year. Notably, the full-depth crack in the microCT image of the 25 x 25 x 25 mm³ OPC paste sample (Fig. 3b) did not impact the compressive strength of the 75 mm x 150 mm cylindrical mortar and concrete samples. Since paste samples consist solely of hydrated binder without aggregates, they are more reactive and exhibit lower resistance to cracking compared to mortar samples. Additionally, small paste samples have a higher surface-to-volume ratio than cylindrical ones, leading to faster seawater diffusion. This led to increased exposure effects in the paste samples, which may weaken the mechanical strength of the cylinders in the next couple of years.

As depicted in Fig. 7b, the initial splitting tensile strengths of the RRC and AAM before exposure were 1.9 MPa and 1.4 MPa, respectively, which are comparatively low compared to the OPC's strength of 2.8 MPa. For all batches except AAM, the 1-year strength was within the 5-month strength's error bar, showing no statistically significant variation. OPC achieved the highest strength, approximately 4 MPa. RRC and AAM mortar samples demonstrated similar strengths, around 3 MPa. Interestingly, while AAM did not show improved compressive strength, its tensile strength significantly increased after one year of exposure. This anomaly requires further analysis for clarification.

Environmental impact of different binder systems under seawater exposure

Figure 8 shows the global warming potential (GWP) results of different mortar samples containing RRC, OPC, and AAM as the binder. The target compressive strength of the mortars was 30 MPa after 28 days of laboratory curing. Accordingly, the GWP of the mortar mixes required to produce 1 m³ of mortar was calculated both with and without considering the target strength as a functional parameter, as shown in Fig. 8a, b, respectively. The results indicated that RRC and AAM mortars achieved approximately 59% and 72% reductions in carbon footprint compared to OPC mortars. While producing 1 m³ of mortar resulted in carbon emissions of 470 kg CO_2 eq for OPC, RRC and AAM exhibited significantly lower emissions—192 kg CO_2 eq and 131 kg CO_2 eq, respectively. However, after 1 year of seawater exposure, the compressive strength of OPC increased substantially. Therefore, when the 1-year compressive strength was used as a functional parameter, the GWP of OPC was calculated as 7 kg CO_2 eq/m³·MPa, whereas RRC and AAM showed values of 3.48 and 3.33 kg CO_2 eq/m³·MPa, respectively (Fig. 8c). As a result, the GWP reduction of RRC and AAM compared to OPC was relatively lower, 50% and 52%, respectively. Despite having low compressive strength and requiring a higher binder content to achieve 1 MPa compressive strength, RRC and AAM showed significant GWP reduction because of lower energy requirements for their raw ingredients processing. Among the raw materials used in RRC, lime production contributed the most to carbon emissions. Additionally, the need for superplasticizers to enhance the workability of RRC—partly due to kaolin's high specific surface area—also contributed to the increase in GWP. In the case of AAM, using NaOH as the alkali activator significantly contributed to its GWP increase. While slag served as the precursor for this binder, its impact was comparatively less due to being an industrial byproduct.

Evaluation of the bio-receptivity of the binder composites

Figure 9 illustrates the physical condition of mortar samples, focusing on biological growth on their surface after natural seawater exposure for up to 1 year. After 1 month, all binder systems showed barnacle formation; among them, OPC mortar had less biological growth than RRC and AAM mortars (Fig. 9a, d, g). However, barnacle growth increased in all the samples in the

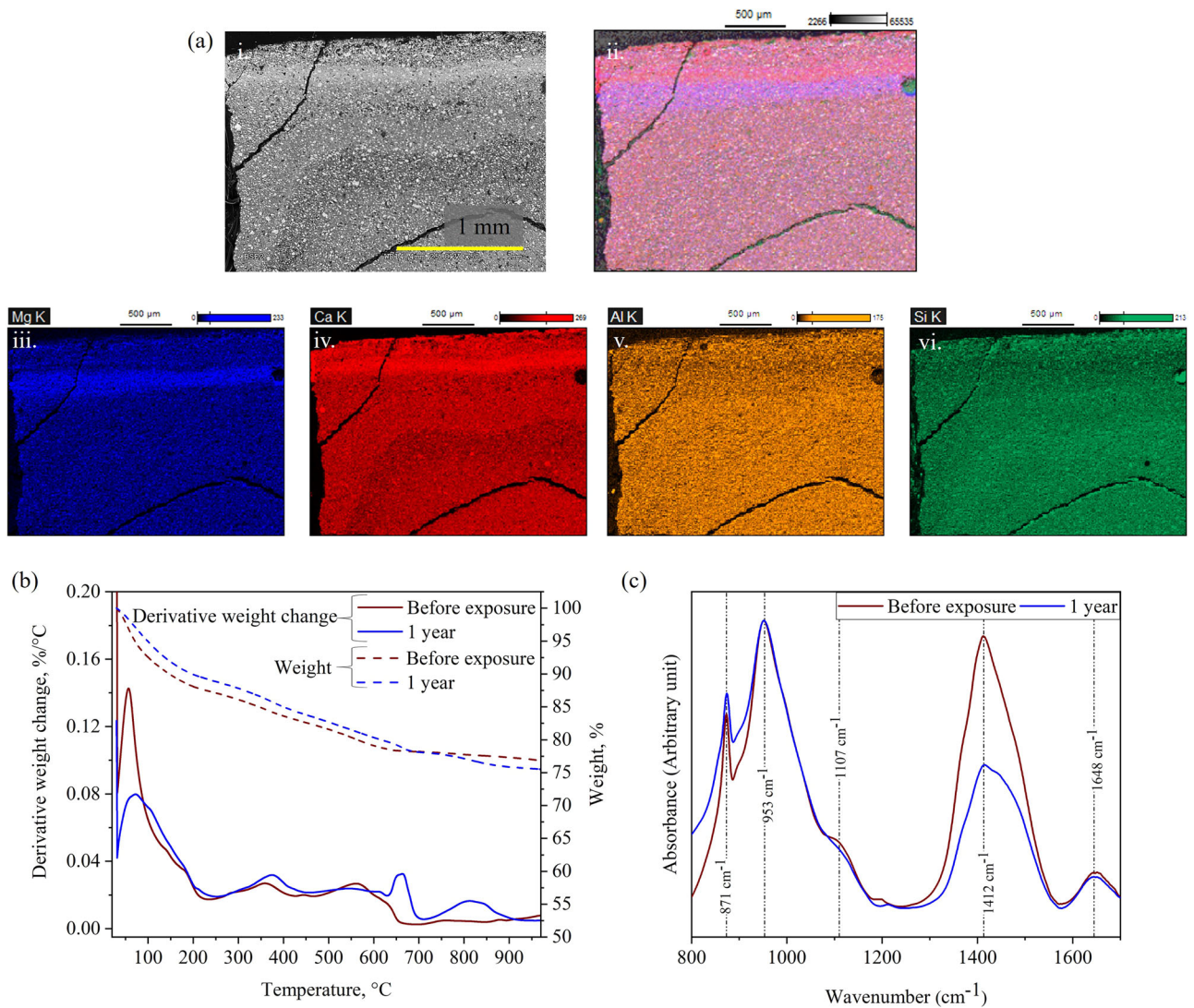


Fig. 6 | Compositional evolution in the AAM peripheral region under 1-year seawater exposure. a Elemental variation (1-year exposure), **b** TG-DTG curve (before exposure and 1-year exposure), and **c** FTIR spectra (before exposure and 1-year exposure) of the AAM peripheral region.

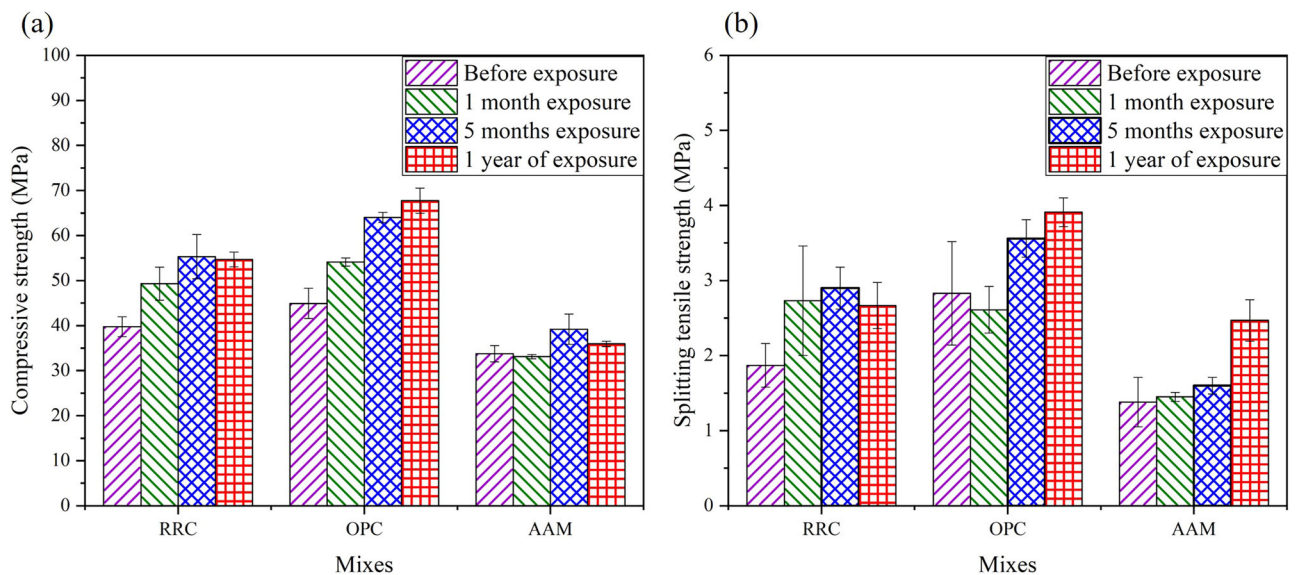


Fig. 7 | Mechanical property evaluation of mortars exposed to seawater for different durations of up to one year. a Compressive and **b** splitting tensile strengths of mortars.

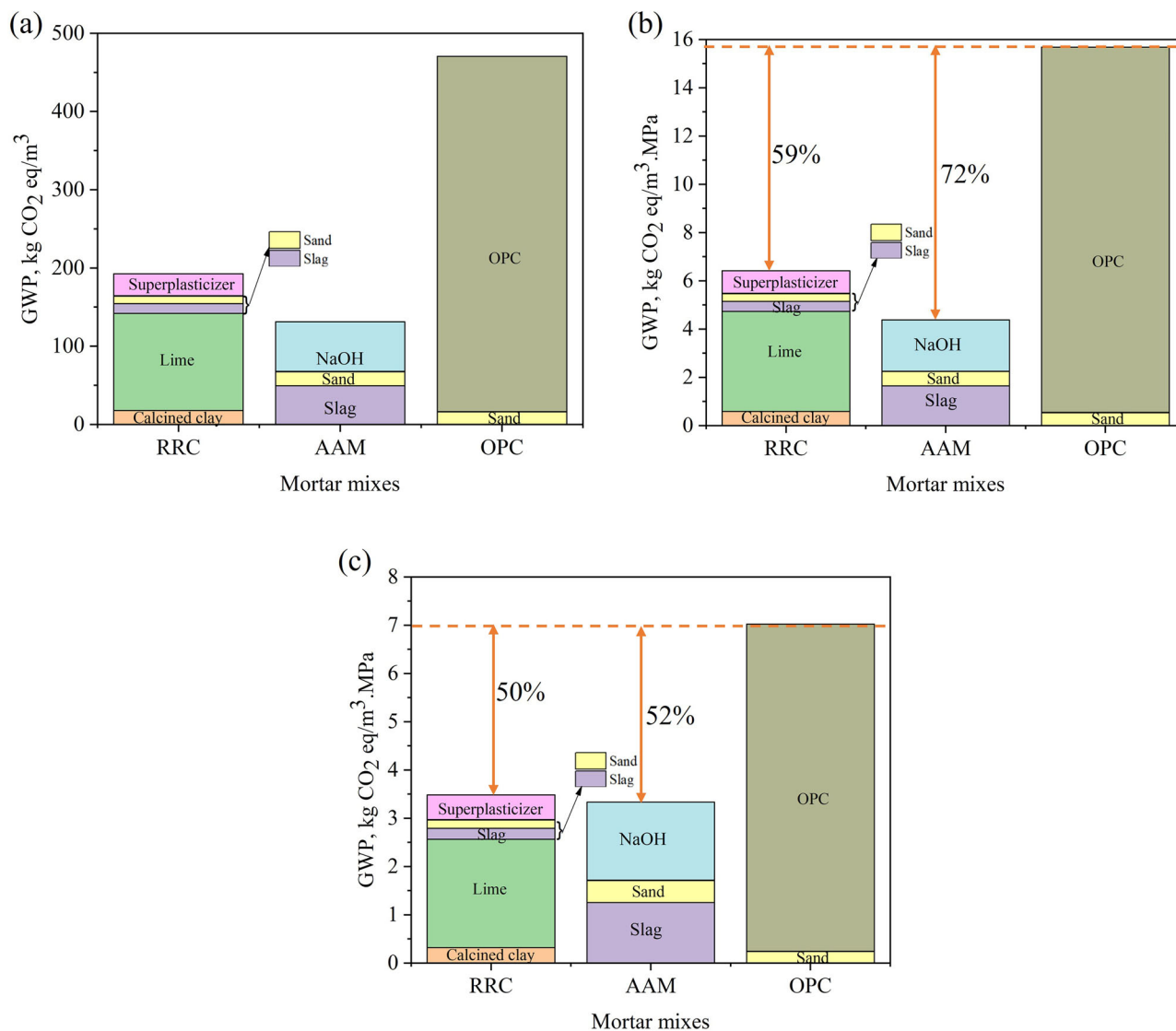


Fig. 8 | Global warming potential of different mortar mixes. The functional unit considered: **a** kg/m³, **b** kg/m³. MPa (considering target strength 30 MPa), **c** kg/m³. MPa (considering 1-year compressive strength).

later exposure durations (5 months and 1 year) (Fig. 9b, c, e, f, h, i). Additionally, the samples submerged in seawater for an extended period also demonstrated the presence of polychaetes (Fig. 9b, c, e, f, h, i). The mineralized tube observed on the mortar surfaces built by these sandcastle worms (polychaetes) consists of sand and shell particles bound by a cement secreted from the worm's thorax⁶¹. These polychaetes enhance reef complexity by creating environmental heterogeneity, which promotes biodiversity by providing new niches for various species⁶². Rough surfaces from polychaete formations may attract more barnacles by enhancing friction and improving the bond stability between the concrete and the barnacles⁶³. Additionally, barnacle cyprids prefer hiding in folds or crevices for protection from predators⁶³. Figure 9j, k, l show BSE images of the barnacle shell on the surface of different paste samples. The point EDS analysis showed the composition of these shells as calcium carbonates. The part of the shells positioned on the binder surface is named the "calcareous base plate," and the other is called the "calcareous wall." Barnacles utilize a proteinaceous adhesive known as barnacle cement to securely attach their bodies to nearly any substrate underwater, allowing them to adhere firmly in aquatic environments. Fig. S6 (Supplementary section) shows the existence of the adhesive glue on the edge of the barnacle; a darker region can be seen in these images on which whitish depositions are visible. The EDS shows that the darker region has phosphorus (P) and nitrogen (N) in it, and the whitish

region on it is the deposition of NaCl crystals absorbed from the seawater. It can be inferred that the barnacles were cemented on the sample using this glue, and at the periphery of the barnacles, NaCl crystals adhered to this adhesive. The shells, along with their adhesive layer and the penetration of this adhesive, function as three lines of defense that safeguard concrete from the harsh marine environment^{31,63}. Throughout these assessments, no damage to the samples due to the barnacle or other marine organism growth was observed, indicating all these composites could serve as substrates for artificial reefs while also providing coastal protection.

To evaluate the efficiency of different binder systems from this study as a substratum for oyster development, hatchery-spawned oysters were settled and grown on paste samples in the laboratory for 16 weeks. Within 1 week, RRC and AAM showed signs of biological growth on their surfaces (Fig. 10a, c). Over time, the RRC exhibited the most substantial growth of oysters, fully covering its surface after 16 weeks (Fig. 10a). The AAM also displayed moderate growth after 16 weeks (Fig. 10c), in contrast to the OPC sample, which showed reduced signs of oyster development (Fig. 10b). Previous literature indicates that the pearl oyster, *Pinctada martensii*, exhibits a strong preference for darker substrates when settling, suggesting that habitat coloration plays a significant role in its settlement behavior⁶⁴. Having a colored surface (Fig. 10a) may explain the higher settlement and growth on RRC. In contrast, AAM and OPC are primarily whitish or greyish

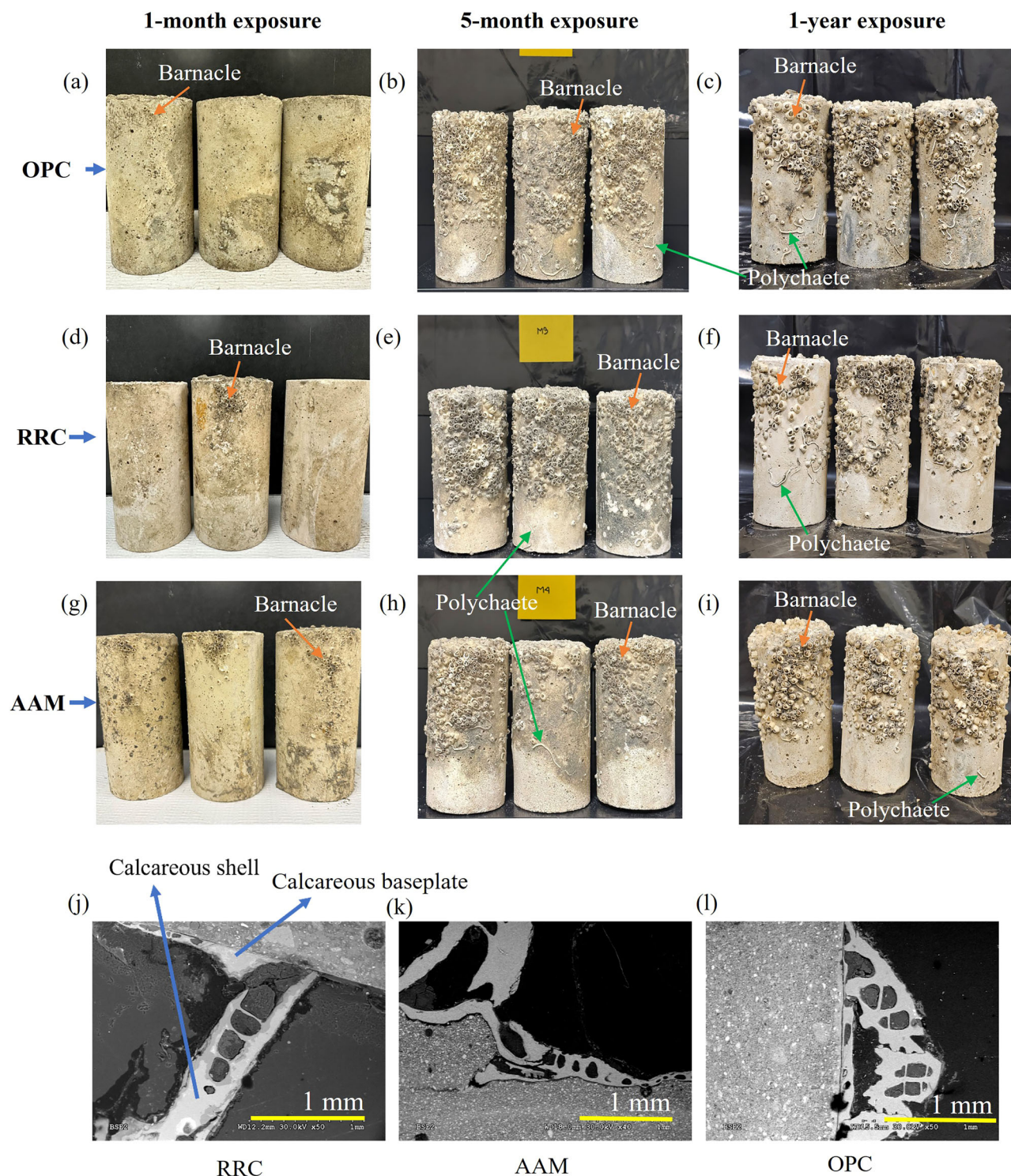


Fig. 9 | Biological growth on different cementitious substrates at different exposure durations. Barnacle and polychaete growth on OPC after (a) 1-month, b 5-month, c 1-year; on RRC (d) 1-month, e 5-month, f 1-year; on AAM (g) 1-month, h 5-month, i 1-year. BSE images of the barnacle shell on different samples (j) RRC, k AAM, l OPC.

in color (Supplementary section, Fig. S7b, c), which may have influenced the lower biological growth. However, porosity and surface roughness also play a crucial role in enhancing colonization⁶⁵. Increasing porosity enhances moisture retention and the deposition of organic and inorganic particles, referred to as extrinsic bio-receptivity, while intrinsic bio-receptivity involves using pore spaces for spore deposition and as habitats for biofilm taxa⁶⁵. MicroCT analysis revealed that RRC had a higher number of air voids (Fig. 3a-vii), which possibly provided a more suitable attachment surface for

the oyster larvae. Biological precipitation typically favors low pH substrates, while OPC and AAM are high pH cementitious systems, with pore solution pH values of 12.6–13.5 and 13–13.8, respectively⁶⁶. In contrast, the pore solution pH of RRC was measured at 10.9; the methodology for pH determination is detailed in Supplementary Section 2. Therefore, it is hypothesized that the high alkalinity of OPC and AAM surfaces may have inhibited oyster growth, whereas the comparatively lower pH of RRC provided a more favorable environment for biological attachment.

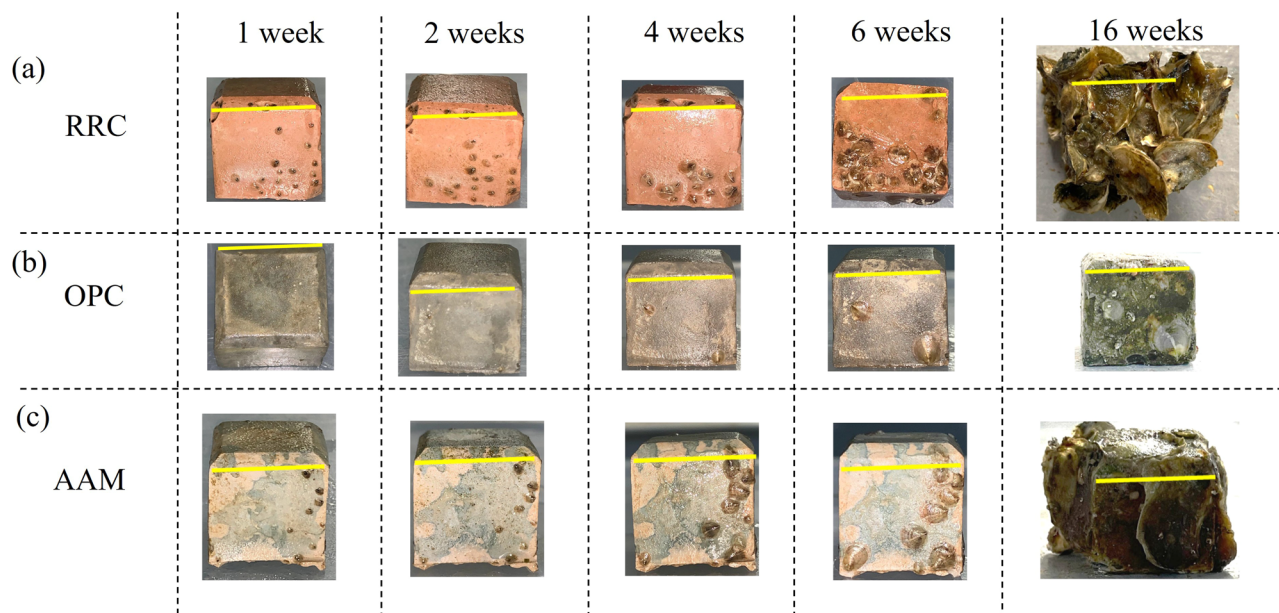


Fig. 10 | Oyster growth on substrates with different binder systems. a RRC, b OPC, c AAM. The yellow scale bar shows 25 mm.



Fig. 11 | Location of sample placements for field exposure testing. Map indicating the location of sample placements at Baffin Bay, Texas.

However, more detailed study with a larger sample number is required to fully assess the bio-receptivity of different cementitious composites.

Discussions

This study suggests that cementitious materials, including recreated Roman cement (RRC) and alkali-activated materials (AAM), can effectively serve as substrates for marine biological growth. This capability could play a significant role in restoring the marine ecological environment, while also demonstrating impressive durability for marine structures.

In the RRC system, cementation occurs through a pozzolanic reaction between $\text{Ca}(\text{OH})_2$ and calcined clay in the presence of seawater. Previous literature indicates that this reaction forms C-A-S-H, stratlingite (C_2ASH_8),

and C_4AH_{13} ⁶⁷. When exposed to seawater, these compounds bound Cl^- and SO_4^{2-} ions, forming ettringite and hydrocalumite²⁰, as observed in Fig. 1a. Mineral crystallization primarily took place during the early stages, leading to $\text{Ca}(\text{OH})_2$ depletion, which was added as a raw material (Fig. 1a). As a result, the formation of delayed ettringite or other damaging sulfate-bearing phases, such as gypsum or thaumasite, was not detected in the XRD analysis of the 1-year-old RRC samples (Fig. 1a). Additionally, the crystallization at an early age contributed to pore refinement and gel precipitation around these crystals, ultimately creating a dense microstructure with fewer large capillary voids (Fig. 2d). Consequently, RRC imparted around 55 MPa compressive strength after 1 year of seawater exposure without showing any significant decrease in compressive and splitting tensile strength over time

(Fig. 7a). However, the microCT analysis shows large air voids remaining (0.55% of the total volume), which can be due to the stiff RRC mix trapping the air from escaping during compaction (Fig. 3a–vii). These air voids, along with the colored surface and low pH of RRC (pH=10.9), likely provided a suitable surface for oyster larvae attachment^{61,62}, leading to the highest oyster growth on RRC (Fig. 10a). Additionally, microCT images of the RRC matrix cross-sections showed that RRC samples exhibited the least damage in terms of crack formation after one year of exposure (Fig. 3a). Nonetheless, a continuous increase in hydrotalcite formation was detected in the peripheral region over time (Fig. 4). RRC, being rich in Al and Mg, along with the intrusion of Mg from seawater, resulted in the formation of Mg and Al-based layered double hydroxide solids (Mg–Al-LDH) or hydrotalcite; additionally, the inclusion of CO_3^{2-} from seawater increased the stability and crystallinity of this hydrotalcite⁶⁸.

In the AAM system, a higher pH of the pore solution boosts its activation and hydration by enhancing slag dissolution via hydroxide ions (OH^-)¹⁸. Longer seawater exposure broadened the C–S–H peak of AAM, indicating enhanced slag dissolution and increased C–S–H formation (Fig. 1c and Fig. S1c). Additionally, the MIP results supported this observation, showing a reduction in the initially present capillary pores and an increase in gel pores (Fig. 2f). Overall, AAM exhibited the lowest cumulative pore volume compared to the other two binder systems (Fig. 2c). This characteristic resulted in a very dense microstructure, leading to high capillary pressures during the drying process in the sealed curing period (before seawater curing), which significantly increased shrinkage. The microCT analysis of the AAM sample revealed surface cracks propagating throughout the microstructure, suggesting that they are shrinkage cracks (Fig. 3c–iii, vi). As early-age curing in water can lead to leaching of key constituents required for the strength development of AAM⁵¹, initial curing was done in a sealed curing condition. However, this approach led to the formation of drying shrinkage cracks, ultimately resulting in reduced compressive strength of this sample. After one year, the AAM mortar reached only 35 MPa (Fig. 7a), despite previous studies indicating that AAM has the potential to develop significant compressive strength when exposed to seawater⁴⁴. Analysis of the peripheral region of the sample revealed a stable increase in calcite formation along with a Mg-rich zone (Fig. 6a), suggesting potential carbonation of C–S–H and a corresponding increase in M–S–H adjacent to the areas of CaCO_3 deposition. Important to note that, typically, the performance of AAM varies significantly depending on the precursor and activators used. Therefore, although the AAM mixture provided the lowest compressive strength in this study, design optimization of AAM can be incorporated to achieve better performance in the marine environment.

OPC hydration led to the continuous $\text{Ca}(\text{OH})_2$ formation, which bound SO_4^{2-} ions from seawater, facilitating the ongoing formation of gypsum and ettringite over time (Fig. 1b). Soluble carbonates in seawater caused calcite and thaumasite formation in the OPC matrix after 5 months and 1 year (Fig. 1b). Thaumasite was absent in the samples before exposure but likely developed during winter as the temperature drop facilitated its formation (Fig. 5b). In addition to the thaumasite layer, the outermost region of this sample consists of a CaCO_3 layer, with a MgCO_3 layer adjacent to its inner side (Fig. 5a). Over time, the SO_4^{2-} and CO_3^{2-} -bearing mineral formations in the OPC matrix filled the large capillary pores (Fig. 2e) observed in the before-exposure sample. Overall, OPC demonstrated the highest compressive strength among all the binder systems, achieving around 70 MPa compressive strength after 1 year. Despite having high strength, OPC ultimately resulted in the highest CO_2 emissions among all the binder systems studied due to requiring an energy-intensive clinker process. Additionally, the production of thaumasite, alongside the delayed ettringite and gypsum formation, resulted in the OPC matrix degradation. MicroCT imaging revealed the presence of full-depth crack formation within the OPC matrix. Furthermore, the OPC sample, which exhibited considerably less oyster settlement and development (Fig. 10b), could be attributed to its high pH binder environment due to the presence of Ca^{2+} in the pore solution.

Methods

Raw materials and sample preparation

This study evaluates the macrostructural and microstructural properties of mortar and paste samples with different binders when exposed to natural seawater conditions. In the calcined clay–portlandite binder (i.e., RRC), the portlandite-to-clay ratio was kept at 1:3, and 20% of the calcined clay was replaced by slag. Notably, medium-grade kaolin clay having 50–60% kaolin content was used in the RRC binder. The clay was calcined at 750 °C for 6 h using a muffle furnace with a rising rate of 4 °C/min. The AAM samples were prepared by activating blast furnace slag with sodium hydroxide (NaOH) at a 5% Na_2O dosage (by weight of the binder). Only the RRC mixes utilized a superplasticizer at a dosage of 2% by binder mass. Seawater was utilized to produce the RRC and OPC mixes. It's important to recognize that different cement-based systems—such as geopolymers and Portland cement—require distinct design strategies due to their fundamentally different hardening processes. For instance, some geopolymer composites may need high-temperature curing to reach strength levels comparable to OPC. Applying the same mix design and curing conditions across all samples in this study would likely result in uneven initial performance (before seawater exposure), making it difficult to isolate the effects of seawater itself. To ensure a fair comparison and achieve a consistent target strength of 30 MPa, each cementitious system was tailored with specific curing methods and mix proportions. AAMs are complex systems and are sensitive to the combinations of precursors and activators used³⁵. Previous literature shows that the compressive strength of AAMs mixed with seawater varies minimally (5–6%) compared to those mixed with freshwater^{18,34,69,70}. To reduce initial variability, freshwater was used for AAM mixes. The oxide content of the raw materials was determined using X-ray fluorescence (XRF) analysis and is shown in Table 1. Table 2 depicts the mixture proportions.

To determine the mechanical properties, including compressive and flexural strength, mortar cylinders with a diameter of 75 mm and a height of 150 mm were prepared. Mortar samples were prepared, including RRC, AAM, and OPC as binders, to compare their mechanical performance and assess their potential application in additive manufacturing. 25 x 25 x 25 mm³ paste cubes, excluding sand, were prepared for microstructural analysis following the same mix design as the mortar samples.

Exposure conditions

The mortar and paste samples were prepared in the laboratory and underwent an initial curing period of 28 days. Artificial seawater, prepared by dissolving 680 g of sea salt (Instant Ocean) in 18.9 L of water, was used for the initial curing of RRC and OPC samples. Its chemical composition, shown in Table S1 (Supplementary section), is representative of ocean water⁷¹ and complies with ASTM D1141⁷². Initial curing for AAM samples was done in a sealed condition. Although AAM has the capacity to be used in seawater concrete and can develop considerable compressive strength when exposed to seawater³⁴, early-age curing in water can lead to leaching of key constituents⁵¹, which adversely impacts the durability and performance of the binder system. Therefore, to prevent this leaching and to allow proper development of the reaction products, initial curing was done in a sealed condition. This method aligns with prior studies using sealed or moist curing for 28 days before seawater exposure^{18,73}. Notably, the initial curing condition will be referred to as 'before exposure' later in this study. Afterward, the samples were carefully delivered to Baffin Bay, Texas, to be submerged in natural seawater for one year, experiencing seasonal temperature fluctuations (Fig. 11). Samples were retrieved after 1 month, 5 months, and 1 year of exposure, then properly air-dried prior to characterization. The mechanical and microstructural properties of both the "before exposure" samples and those exposed to seawater were subsequently evaluated.

Material characterization techniques

X-ray diffraction analysis (XRD) was employed to identify the hydration reaction products in paste samples using a Bruker D-8 spectrometer. It operated at 40 kV and 40 mA, utilizing Cu K α radiation with a step size of 0.03° per second and a 2 θ range of 5° to 60°. The sampling involved

pulverizing entire paste samples uniformly and passing them through a 75 μm sieve.

The pore structures of different binder systems under seawater exposure were characterized using Mercury Intrusion Porosimetry (MIP) conducted with the Micromeritics Instrument Corporation AutoPore IV 9500 V2.03.01. Mercury with a surface tension of 0.485 N/m and a contact angle of 130 degrees was used, with pressure increased to 413 MPa to inspect pores as small as 3.02 nm in diameter. The sample size was standardized to 15 x 15 x 15 mm³.

The X-ray micro-computed tomography (microCT) test was performed with a high-resolution μCT scanner (μCT 45, Scanco Medical, Brüttisellen, Switzerland) to evaluate macro pore distribution and microstructural changes across cross-sections. The experiment had a resolution of 48 μm , indicating that the smallest detected pixel size was over 48 μm . X-rays were emitted at 55 kVp and 145 μA while scanning 25 x 25 x 25 mm³ paste cubes, generating around 600 TIFF images. These images were stacked using the Object Research System (ORS) Dragonfly Pro software to reconstruct 3D grayscale images. Grey-scale intensity ranges were employed to effectively segment the phases within the samples. This process involved distinguishing the voids from solid materials as well as differentiating between various solid phases based on their specific pixel variations using the advanced modules (multiscale ROI) available in Dragonfly software.

Thermogravimetric (TGA) analysis was performed on cement paste powders using a TGA 550 TA instrument in a dry nitrogen atmosphere. The samples weighing 30–40 mg were heated to 980 °C at a constant rate of 15 °C/min after a 3 min isothermal hold. The microstructural evolution in the paste samples due to long-term seawater exposure is expected to be most pronounced in the peripheral region, as indicated by the observed layering in that area (Supplementary section, Fig. S8). Therefore, sampling for TGA analysis was conducted on the peripheral region of the paste sample. Additionally, TGA results from powder obtained by uniformly grinding the entire paste sample are provided in the Supplementary section (Fig. S1).

Fourier Transform Infrared Spectroscopy (FTIR) analysis was performed using a Nicolet iS5 FTIR spectrometer with an ATR accessory at 4 cm⁻¹ resolution. Each spectrum averaged 32 scans over frequencies from 400 to 4000 cm⁻¹. Sampling for this test was also conducted from the peripheral region of the paste sample, similar to the TGA analysis.

Scanning electron microscopy (SEM) images were obtained with a HITACHI 3000 N SEM at 25–30 kV. For BSE analysis, low-viscosity epoxy-coated polished samples were gold-palladium coated. Area mapping with an energy-dispersive X-ray spectrometer (EDS) was used to confirm the elemental distribution in the peripheral region of the 1-year seawater-exposed samples.

The mechanical properties of the 75 mm x 150 mm cylindrical mortar samples were evaluated using a universal testing machine. ASTM C1550 was followed for performing the flexural strength test, and the splitting tensile strength test was conducted according to ASTM C496. The average strength of three mortar samples was calculated to determine the overall mortar strength.

Life cycle analysis

Life cycle analysis of the mortar samples with different binder systems, including RRC, OPC, and AAM, was conducted using SimaPro 9.0.0.48. The GWP of most raw materials was derived from the Ecoinvent 3 dataset (Table 3) and the impact assessment was done using the Tool for the Reduction and Assessment of Chemical and Other Environmental Impacts (TRACI). Emissions from clay processing—extraction, transportation, calcination, and ball milling—were incorporated into SimaPro manually. The input data for clay extraction and transportation were sourced from the clay inventory in the ecoinvent 3 database, chosen for its accessibility. However, further studies are needed to refine the analysis by considering the specific kaolin deposit location and the distance to the processing plant. Additionally, the clay calcination energy data were collected from previous literature^{74,75}. According to the simaPro analysis using these data, the clay processing emits 0.032 kg CO₂ eq/kg. A previous study found that in the

RRC system, natural hydraulic lime (NHL 2) performs similarly to hydrated lime. Therefore, being a low-carbon lime source, the GWP for NHL 2 was used for the GWP calculation of RRC mortars. Among the other binders, OPC production was found to be carbon-intensive, emitting 0.915 kg CO₂ eq/kg. Whereas, in slag-based AAM systems, ground granulated blast furnace slag (GGBFS) has a minimal GWP due to its status as an industrial byproduct⁷⁶, with a carbon footprint of 0.091 kg CO₂ eq/kg from processes including granulation, drying, crushing, grinding, and storage. However, its activation with NaOH, which emits 1.915 kg CO₂ eq/kg, increases the overall AAM GWP⁷⁷. Lastly, the functional parameter used for this study was the material required for producing a 1 m³ mortar with 1 MPa compressive strength. In this study, transportation emissions of raw materials were excluded from the carbon footprint calculations for mortar mixes, as they are location-specific and can vary significantly. This approach allows for a more consistent comparison of the environmental impact of different mortar systems by focusing on emissions from raw material production.

Oyster culture procedure

To assess the suitability of various binder systems as substrates for oyster growth, oyster larvae were cultured on 25 x 25 x 25 mm³ paste cubes at the Texas A&M AgriLife Mariculture Research Facility, using procedures described in previous studies^{78–80}. The detailed larvae culture methodology is shown in Section S1 (Supplementary section). The substrates were removed and photographed at 1, 2, 4, 6, and 16 weeks after settlement.

Data availability

All data will be available upon request.

Received: 22 March 2025; Accepted: 20 July 2025;

Published online: 24 September 2025

References

- Lee, K. & Jepson, W. Environmental impact of desalination: a systematic review of Life Cycle Assessment. *Desalination* **509**, 115066 (2021).
- Ren, J. et al. A comparison between alkali-activated slag/fly ash binders prepared with natural seawater and deionized water. *J. Am. Ceram. Soc.* **105**, 5929–5943 (2022).
- Eltawil, M. A., Zhengming, Z. & Yuan, L. A review of renewable energy technologies integrated with desalination systems. *Renew. Sustain. Energy Rev.* **13**, 2245–2262 (2009).
- Wu, W. et al. Characteristics of the alkali-silica reaction in seawater and sea sand concrete with different water-cement ratios. *Constr. Build. Mater.* **400**, 132822 (2023).
- Wang, Q. et al. Feasibility assessment and application of sea sand in concrete production: a review. *Structures* **60**, 105891 (2024).
- Santhanam, M., Cohen, M. & Olek, J. Differentiating seawater and groundwater sulfate attack in Portland cement mortars. *Cem. Concr. Res.* **36**, 2132–2137 (2006).
- Andrew, R. M. Global CO₂ emissions from cement production. *Earth Syst. Sci. Data* **10**, 195–217 (2018).
- Monkman, S., Sargam, Y. & Raki, L. Comparing the effects of in-situ nano-calcite development and ex-situ nano-calcite addition on cement hydration. *Constr. Build. Mater.* **321**, 126369 (2022).
- Smith, L., Cornillon, P., Rudnickas, D. & Mouw, C. B. Evidence of environmental changes caused by Chinese island-building. *Sci. Rep.* **9**, 5295 (2019).
- Ting, M. Z. Y. & Yi, Y. Durability of cementitious materials in seawater environment: A review on chemical interactions, hardened-state properties and environmental factors. *Constr. Build. Mater.* **367**, 130224 (2023).
- Yi, Y., Zhu, D., Guo, S., Zhang, Z. & Shi, C. A review on the deterioration and approaches to enhance the durability of concrete in the marine environment. *Cem. Concr. Compos.* **113**, 103695 (2020).
- Jakobsen, U. H., De Weerd, K. & Geiker, M. R. Elemental zonation in marine concrete. *Cem. Concr. Res.* **85**, 12–27 (2016).

13. Stark, J. & Bollmann, K. Delayed ettringite formation in concrete. *Nord. Concr. Res. Publ.* **4**, 28 (2000).
14. Cheng, S. et al. Degradation mechanisms of Portland cement mortar under seawater attack and drying-wetting cycles. *Constr. Build. Mater.* **230**, 116934 (2020).
15. Zhang, Y. et al. Long-term investigation of alkali-silica reaction behaviors in seawater sea-sand concrete. *Cem. Concr. Compos.* **151**, 105611 (2024).
16. Puertas, F., De Gutiérrez, R., Fernandez-Jimenez, A., Delvasto, S. & Maldonado, J. Alkaline cement mortars. Chemical resistance to sulfate and seawater attack. *Mater. Constr.* **52**, 55–71 (2002).
17. Zhang, B., Zhu, H., Shah, K. W., Feng, P. & Dong, Z. Optimization of mix proportion of alkali-activated slag mortars prepared with seawater and coral sand. *Constr. Build. Mater.* **284**, 122805 (2021).
18. Jun, Y., Kim, J. H., Han, S. H. & Kim, T. Influence of seawater on alkaliactivated slag concrete. *Mater. Struct./Mater. Constr.* **54**, 121 (2021).
19. Ashraf, W. et al. Mimicking the cementation mechanism of ancient Roman seawater concrete using calcined clays. *Appl. Clay Sci.* **230**, 106696 (2022).
20. Tahsin, A., Siddique, S., Ashraf, W. & Sattler, M. Assessment of the durability and environmental impact of seawater-activated portlandite-calcined clay binder. *J. Sustain. Cem. Based Mater.* **12**, 1564–1576 (2023).
21. Palomo, A., Monteiro, P., Martauz, P., Bilek, V. & Fernandez-Jimenez, A. Hybrid binders: a journey from the past to a sustainable future (opus caementicium futurum). *Cem. Concr. Res.* **124**, 105829 (2019).
22. Tahsin, A. & Ashraf, W. Unveiling the carbon footprint reduction potential of cementitious composites: CO₂ sequestration in a lime-clay binder incorporating medium-grade clay. *ACS Sustain. Chem. Eng.* **12**, 11099–11110 (2024).
23. Tahsin, A., Borno, I. B. & Ashraf, W. Influence of different lime sources on the properties and environmental impacts of seawater-activated lime-calcined clay binder. *J. Sustain. Cem. Based Mater.* **14**, 36–947 (2025).
24. Natanzi, A. S., Thompson, B. J., Brooks, P. R., Crowe, T. P. & McNally, C. Influence of concrete properties on the initial biological colonisation of marine artificial structures. *Ecol. Eng.* **159**, 106104 (2021).
25. Guilbeau, B. P., Harry, F. P., Gambrell, R. P., Knopf, F. C. & Dooley, K. M. Algae attachment on carbonated cements in fresh and brackish waters—preliminary results. *Ecol. Eng.* **20**, 309–319 (2003).
26. Teong, T. K. et al. Marine bioreceptivity among green concretes. *Ecol. Eng.* **204**, 107284 (2024).
27. Coombes, M. A., Viles, H. A., Naylor, L. A. & La Marca, E. C. Cool barnacles: Do common biogenic structures enhance or retard rates of deterioration of intertidal rocks and concrete? *Sci. Total Environ.* **580**, 1034–1045 (2017).
28. Lv, J. F., Mao, J. Z. & Ba, H. J. Influence of *Crassostrea gigas* on the permeability and microstructure of the surface layer of concrete exposed to the tidal zone of the Yellow Sea. *Biofouling* **31**, 61–70 (2015).
29. Chlayon, T., Iwanami, M. & Chijiwa, N. Combined protective action of barnacles and biofilm on concrete surface in intertidal areas. *Constr. Build. Mater.* **179**, 477–487 (2018).
30. Lv, J., Mao, J. & Ba, H. Influence of marine microorganisms on the permeability and microstructure of mortar. *Constr. Build. Mater.* **77**, 33–40 (2015).
31. Lv, J., Cao, Z. & Hu, X. Effect of biological coating (*Crassostrea gigas*) on marine concrete: Enhanced durability and mechanisms. *Constr. Build. Mater.* **285**, 122914 (2021).
32. De Weerd, K., Justnes, H. & Geiker, M. R. Changes in the phase assemblage of concrete exposed to sea water. *Cem. Concr. Compos.* **47**, 53–63 (2014).
33. Ragab, A. M., Elgammal, M. A., Hodhod, O. A. G. & Ahmed, T. E. S. Evaluation of field concrete deterioration under real conditions of seawater attack. *Constr. Build. Mater.* **119**, 130–144 (2016).
34. Mengasini, L., Mavroulidou, M. & Gunn, M. J. Alkali-activated concrete mixes with ground granulated blast furnace slag and paper sludge ash in seawater environments. *Sustain. Chem. Pharm.* **20**, 100380 (2021).
35. Liu, W., Zhao, J., Feng, Y., Zhang, B. & Xie, J. Seawater-mixed alkaliactivated materials: a state-of-the-art review. *J. Mater. Sci.* **60**, 2169–2198 (2025).
36. Borno, I. B., Tahsin, A. & Ashraf, W. Utilization of industrial waste sodium sulfate for calcined clay-based sustainable binder. *Constr. Build. Mater.* **440**, 137073 (2024).
37. Frías, M. & Cabrera, J. Influence of MK on the Reaction Kinetics in MK/Lime and MK-Blended Cement Systems at 20 °C. *Cem. Concr. Res.* **31**, 519–527 (2001).
38. Yoon, S. et al. Chloride adsorption by calcined layered double hydroxides in hardened Portland cement paste. *Mater. Chem. Phys.* **145**, 376–386 (2014).
39. Shi, Z. et al. Friedel's salt profiles from thermogravimetric analysis and thermodynamic modelling of Portland cement-based mortars exposed to sodium chloride solution. *Cem. Concr. Compos.* **78**, 73–83 (2017).
40. Yamaguchi, T., Sawaguchi, T., Tsukada, M., Hoshino, S. & Tanaka, T. Mineralogical changes and associated decrease in tritiated water diffusivity after alteration of cement–bentonite interfaces. *Clay Min.* **51**, 279–287 (2016).
41. Kang, C. & Kim, T. Effect of reverse-osmosis brine and sodium aluminate on the hydration properties and strength of alkali-activated slag cement. *Case Stud. Constr. Mater.* **16**, e01078 (2022).
42. Ram, K., Flegar, M., Serdar, M. & Scrivener, K. Influence of low- to medium-kaolinite clay on the durability of limestone calcined clay cement (LC3) concrete. *Materials* **16**, 1–18 (2023).
43. Christensen, A. N., Jensen, T. R. & Hanson, J. C. Formation of ettringite, Ca(6)Al(2)(SO₄)₃(OH)(12)·26H₂O, AFt, and monosulfate, Ca(4)Al(2)O(6)(SO₄)·14H₂O, AFm-14, in hydrothermal hydration of Portland cement and of calcium aluminum oxide - Calcium sulfate dihydrate mixtures studied by in situ synchrotron X-ray powder diffraction. *J. Solid State Chem.* **177**, 1944–1951 (2004).
44. *Lea's Chemistry of Cement and Concrete*. (Butterworth-Heinemann, 2019).
45. Bensted, J. Thaumassite-background and nature in deterioration of cements, mortars and concretes. *Cem. Concr. Compos.* **21**, 117–121 (1999).
46. Khalifa, A. Z. et al. Advances in alkali-activation of clay minerals. *Cem. Concr. Res.* **132**, 106050 (2020).
47. Haque, M. I., Borno, I. B. & Ashraf, W. Enhancing the properties of carbonation cured gamma dicalcium silicates (γ-C2S) using biomimetic molecules. *J. Sustain. Cem. Based Mater.* **13**, 690–705 (2024).
48. Ran, B., Omikrine-Metalssi, O., Fen-Chong, T., Dangla, P. & Li, K. Pore crystallization and expansion of cement pastes in sulfate solutions with and without chlorides. *Cem. Concr. Res.* **166**, 107099 (2023).
49. Fu, J. et al. A microstructural investigation of a Na₂SO₄ activated cement-slag blend. *Cem. Concr. Res.* **150**, 106609 (2021).
50. Cook, R. A. & Hover, K. C. Mercury Porosimetry of Hardened Cement Pastes. *Cem. Concr. Res.* **29**, 933–943 (1999).
51. Liu, C., Wu, H., Li, Z., Shi, H. & Ye, G. Effect of curing condition on mechanical properties and durability of alkali-activated slag mortar. *Constr. Build. Mater.* **439**, 137376 (2024).
52. Mastali, M., Kinnunen, P., Dalvand, A., Mohammadi Firouz, R. & Illikainen, M. Drying shrinkage in alkali-activated binders—a critical review. *Constr. Build. Mater.* **190**, 533–550 (2018).
53. Kaddah, F., Roziere, E., Ranaivomanana, H. & Amiri, O. Complementary use of thermogravimetric analysis and oven to assess the composition and bound CO₂ content of recycled concrete aggregates. *Dev. Built Environ.* **15**, 100184 (2023).
54. Scrivener, K., Snellings, R. & Lothenbach, B. A Practical Guide to Microstructural Analysis of Cementitious Materials. 540 (Boca Raton, FL, USA: CRC press, 2016).

55. Bernard, E., Lothenbach, B., Le Goff, F., Pochard, I. & Dauzères, A. Effect of magnesium on calcium silicate hydrate (C-S-H). *Cem. Concr. Res* **97**, 61–72 (2017).
56. Haque, M. I., Borno, I. B., Khan, R. I. & Ashraf, W. Reducing carbonation degradation and enhancing elastic properties of calcium silicate hydrates using biomimetic molecules. *Cem. Concr. Compos.* **136**, 104888 (2023).
57. Ashraf, W. & Olek, J. Carbonation behavior of hydraulic and non-hydraulic calcium silicates: potential of utilizing low-lime calcium silicates in cement-based materials. *J. Mater. Sci.* **51**, 6173–6191 (2016).
58. Abdalkader, A. H. M., Lynsdale, C. J. & Cripps, J. C. The effect of chloride on cement mortar subjected to sulfate exposure at low temperature. *Constr. Build Mater.* **78**, 102–111 (2015).
59. Matschei, T. & Glasser, F. P. Thermal stability of thaumasite. *Mater. Struct./Mater. Constr.* **48**, 2277–2289 (2015).
60. Corpus Christi Water Temperature and Wetsuit Guide (Texas, USA). <https://www.surf-forecast.com/breaks/Corpus-Christi/seatemp>.
61. Zhao, H., Sun, C., Stewart, R. J. & Waite, J. H. Cement proteins of the tube-building polychaete *Phragmatopoma californica*. *J. Biol. Chem.* **280**, 42938–42944 (2005).
62. Marzalletti, S., Nicoletti, L. & Ardizzone, G. D. The polychaete community of the Fregene artificial reef (Tyrrhenian Sea, Italy): a 20-year study (1981–2001). *Zoosymposia* **2**, 551–566 (2009).
63. Lv, J., Wang, M., Hu, X., Cao, Z. & Ba, H. Experimental study on the durability and microstructure of marine concrete covered with barnacles. *Constr. Build Mater.* **317**, 125900 (2022).
64. Su, Z., Huang, L., Yan, Y. & Li, H. The effect of different substrates on pearl oyster *Pinctada martensii* (Dunker) larvae settlement. *Aquaculture* **271**, 377–383 (2007).
65. Bone, J. R., Stafford, R., Hall, A. E. & Herbert, R. J. H. The intrinsic primary bioreceptivity of concrete in the coastal environment—a review. *Dev. Built Environ.* **10**, 100078 (2022).
66. Wang, Y. et al. Surface characteristics and electrochemical behaviors of passive reinforcing steel in alkali-activated slag. *Corros. Sci.* **190**, 109657 (2021).
67. Gameiro, A., Santos Silva, A., Veiga, R. & Velosa, A. Hydration products of lime-metakaolin pastes at ambient temperature with ageing. *Thermochim. Acta* **535**, 36–41 (2012).
68. Bernard, E., Zucha, W. J., Lothenbach, B. & Mäder, U. Stability of hydrotalcite (Mg–Al layered double hydroxide) in presence of different anions. *Cem. Concr. Res.* **152**, 106674 (2022).
69. Zhao, J., Long, B., Yang, G., Cheng, Z. & Liu, Q. Characteristics of alkali-activated slag powder mixing with seawater: Workability, hydration reaction kinetics and mechanism. *Case Stud. Constr. Mater.* **17**, e01381 (2022).
70. Ren, J. et al. Effects of natural seawater mixing on the properties of alkali-activated slag binders. *Constr. Build Mater.* **294**, 123601 (2021).
71. Pretet, C. et al. Effect of salinity on the skeletal chemistry of cultured scleractinian zooxanthellate corals: Cd/Ca ratio as a potential proxy for salinity reconstruction. *Coral Reefs* **33**, 169–180 (2014).
72. ASTM D 1141. Standard Practice for the Preparation of Substitute Ocean Water. ASTM International, <https://doi.org/10.1520/D1141-98R13> (2003).
73. Zhang, B. & Zhu, H. Compressive stress–strain behavior of slag-based alkali-activated seawater coral aggregate concrete after exposure to seawater environments. *Constr. Build Mater.* **367**, 130294 (2023).
74. Pradhan, S., Chang Boon Poh, A. & Qian, S. Impact of service life and system boundaries on life cycle assessment of sustainable concrete mixes. *J. Clean Prod.* **342**, 130847 (2022).
75. Habert, G. Assessing the environmental impact of conventional and ‘green’ cement production. in *Eco-efficient construction and building materials* 199–238 (2014).
76. Shamass, R., Rispoli, O., Limbachiya, V. & Kovacs, R. Mechanical and GWP assessment of concrete using Blast Furnace Slag, Silica Fume and recycled aggregate. *Case Stud. Constr. Mater.* **18**, e02164 (2023).
77. Turner, L. K. & Collins, F. G. Carbon dioxide equivalent (CO₂-e) emissions: A comparison between geopolymers and OPC cement concrete. *Constr. Build Mater.* **43**, 125–130 (2013).
78. Allen, S. K., Gaffney, P. M., Scarpa, J. & Bushek, D. Inviolate hybrids of *Crassostrea virginica* (Gmelin) with *C. rivularis* (Gould) and *C. gigas* (Thunberg). *Aquaculture* **113**, 269–289 (1993).
79. Scarpa, J. & Allen, S. K. Comparative kinetics of meiosis in hybrid crosses of Pacific oyster *Crassostrea gigas* and Suminoe oyster *C. rivularis* with the American oyster *C. virginica*. *J. Exp. Zool.* **263**, 316–322 (1992).
80. Cresswell, L., Vaughan, D. & Sturmer, L. *Manual for Cultivation of the American Oyster, Crassostrea Virginica, in Florida*. (Fort Pierce, Fla.: Harbor Branch Oceanographic Institution, Tallahassee, FL, 1990).

Acknowledgements

This work was conducted with funding support from the US Defense Advanced Research Projects Agency (DARPA, award # W911NF2010308) at the University of Texas at Arlington. All opinions, findings, and conclusions or recommendations expressed in this material are those of the authors and do not necessarily reflect the views of the sponsor. We gratefully acknowledge Dr. Adnan Rajib and his students for their efforts in organizing the field evaluation of the samples.

Author contributions

Adhara Tahsin: Writing—review and editing, Writing—original draft, Investigation, Formal analysis, Data curation. Ishrat Baki Borno: Writing—review and editing, Investigation, Formal analysis, Data curation. Nishad Ahmed: Data curation. Nithya Nair: Data curation. Warda Ashraf: Writing—review and editing, Supervision, Project administration, Investigation, Funding acquisition, Conceptualization. Christopher Hollenbeck: Writing—review and editing, Investigation.

Competing interests

The authors declare no competing interests.

Additional information

Supplementary information The online version contains supplementary material available at <https://doi.org/10.1038/s41529-025-00652-0>.

Correspondence and requests for materials should be addressed to Warda Ashraf.

Reprints and permissions information is available at <http://www.nature.com/reprints>

Publisher’s note Springer Nature remains neutral with regard to jurisdictional claims in published maps and institutional affiliations.

Open Access This article is licensed under a Creative Commons Attribution-NonCommercial-NoDerivatives 4.0 International License, which permits any non-commercial use, sharing, distribution and reproduction in any medium or format, as long as you give appropriate credit to the original author(s) and the source, provide a link to the Creative Commons licence, and indicate if you modified the licensed material. You do not have permission under this licence to share adapted material derived from this article or parts of it. The images or other third party material in this article are included in the article’s Creative Commons licence, unless indicated otherwise in a credit line to the material. If material is not included in the article’s Creative Commons licence and your intended use is not permitted by statutory regulation or exceeds the permitted use, you will need to obtain permission directly from the copyright holder. To view a copy of this licence, visit <http://creativecommons.org/licenses/by-nc-nd/4.0/>.

© The Author(s) 2025